Tribological Properties of Plasma Sprayed Cr_2O_3, Cr_2O_3-TiO_2, Cr_2O_3-Al_2O_3 and Cr_2O_3-ZrO_2 Coatings

Giovanni Bolelli[1,2,3 *], Daniel Steduto[1,4], Jarkko Kiilakoski[4 §], Tommi Varis[4], Luca Lusvarghi[1,2,3], Petri Vuoristo[4]

[1] Department of Engineering "Enzo Ferrari", Università di Modena e Reggio Emilia, Via Pietro Vivarelli 10/1, 41125 Modena (MO), Italy

[2] InterMech – MO.RE. Centro Interdipartimentale per la Ricerca Applicata e i Servizi nel Settore della Meccanica Avanzata e della Motoristica, Università di Modena e Reggio Emilia, Via Pietro Vivarelli 2, 41125 Modena (MO), Italy.

[3] Consorzio Interuniversitario Nazionale per la Scienza e Tecnologia dei Materiali (INSTM), Local Unit: Università di Modena e Reggio Emilia, Via Pietro Vivarelli 10/1, 41125 Modena (MO), Italy

[4] Tampere University, Faculty of Engineering and Natural Sciences, Materials Science and Environmental Engineering, Surface Engineering Research Group & Thermal Spray Centre Finland (TSCF), P.O. Box 589, FI-33014, Finland

§ Present address: Saint-Gobain Coating Solutions, 50 rue du Mourelet, 84093 Avignon, France

* Corresponding author:
Tel.: +39 0592056233; Fax: +39 0592056243; E-mail: giovanni.bolelli@unimore.it

Abstract

Plasma sprayed Cr_2O_3 is widely used to protect industrial components against wear. The present study seeks to clarify how its properties can be modified by alloying with other oxides. Therefore, pure Cr_2O_3 and Cr_2O_3-25%TiO_2, Cr_2O_3-16%Al_2O_3, Cr_2O_3-35%Al_2O_3, Cr_2O_3-10%ZrO_2 and Cr_2O_3-20%ZrO_2 coatings were studied. All samples were obtained from pre-alloyed feedstock. Cr_2O_3-TiO_2 and particularly Cr_2O_3-Al_2O_3 powders exhibited higher deposition efficiency than did pure Cr_2O_3 and Cr_2O_3-ZrO_2 ones. All coatings consist of supersaturated eskolaite-based solid solutions and small amounts of metallic Cr. Cr_2O_3-ZrO_2 samples also contain cubic and monoclinic ZrO_2.

Compared with pure Cr_2O_3 and Cr_2O_3-Al_2O_3 coatings, the Cr_2O_3-25%TiO_2 and Cr_2O_3-ZrO_2 ones exhibit lower Vickers microhardness but higher toughness, qualitatively assessed by scratch testing.

The sliding wear resistance of the coatings against Al_2O_3 and ZrO_2 balls ranks as their hardness, though ZrO_2 counterparts cause systematically more severe wear. Pure Cr_2O_3 is therefore the most sliding wear resistant of all samples, whilst Cr_2O_3-25%TiO_2 suffers very severe wear.
Dry particles' abrasion, by contrast, is controlled by toughness. The resistance to abrasive wear is, therefore, predicted by scratch testing. The various coatings rank almost the opposite as they did in sliding wear tests, with comparative lower wear losses for Cr_2O_3-25%TiO_2 and (most of all) Cr_2O_3-ZrO_2 samples.

Keywords: Thermal spray coatings; Engineering ceramics; Sliding wear; Two-body abrasion; Hardness.

1. Introduction

Plasma sprayed Cr_2O_3 coatings find numerous industrial applications to provide protection against sliding and abrasive wear. Some relevant examples include papermaking rolls and blades [1], Anilox printing rolls [2], hydraulic seal joints, hydraulic rods and textile rolls [3,4], pump parts including rotors, shaft sleeves, seals, vanes and other wear parts [3,5], and components for high-speed automatic machinery, such as packaging [6] and food processing [7] machinery. Cr_2O_3 is also among the few coating materials that are potentially suited to food-contact applications, because its wear and corrosion resistance minimize the release of undesirable substances into the product [8]. Other extant or potential applications include the protection of cylinder rings in internal combustion engines [9–12], sheet metal punching dies [13], ball valves and seats in hydrometallurgical applications [14].

Alloying Cr_2O_3 with other oxides is a way to modify the properties of the resulting coatings and, to overcome some of the potential limitations involved. Pure Cr_2O_3 coatings are known to have outstanding sliding wear performance [15,16], usually superior to other kind of plasma sprayed oxide ceramic coatings (e.g. Al_2O_3). They can also offer good resistance to other wear processes, e.g. in slurry erosion conditions [17]. However, their brittleness might be an issue, especially when local contact pressures become very high. Indeed, a high-load contact with a hard asperity can trigger wear by macro-fracture [18]. This might impair the coatings' performance e.g. under high-load abrasion [16,19] or dry particles' erosion [20,21] conditions.

Two different alloying strategies have been pursued in the literature and the industrial praxis: either small additions of one or more alloying oxides, or high-alloyed powders.

Cr_2O_3 powders alloyed with small (<5 wt.%) amounts of TiO_2 and/or SiO_2 [22–24] are commercially established materials. They are offered either as fused oxide alloys, mechanical blends, or clad-type powders. In particular, Cr_2O_3 - 5wt.%SiO_2 - 3 / 4wt.%TiO_2 compositions are routinely offered along with pure Cr_2O_3 in the catalogues of thermal spray feedstock manufacturers, some examples of which can be found in [25–27]. These small additions are meant to develop a bit

of glassy phase with low melting point, in order to strengthen the boundary between adjacent lamellae in a coating. They are not supposed to alter the "intrinsic" characteristics of a Cr_2O_3 composition.

Conversely, if Cr_2O_3 is alloyed with a large amount of a second oxide phase, the properties of the resulting material can change remarkably, and open new application possibilities. A few pre-alloyed Cr_2O_3-Al_2O_3, Cr_2O_3-ZrO_2 and Cr_2O_3-TiO_2 feedstock powders are indeed available on the market. However, this avenue has not been explored systematically in the literature. The few extant papers are usually limited to the comparison between pure Cr_2O_3 and one high-alloy system only, the most frequently documented of which is Cr_2O_3-TiO_2. The phase evolution of this system as a function of chemical composition is quite well known. Up to 45 wt.% TiO_2, i.e. on the Cr_2O_3-rich side of interest to the present work, the system reportedly develops an eskolaite-type solid solution (i.e. Ti substituting for Cr in the Cr_2O_3 lattice) and binary phases: $Cr_2Ti_2O_7$, which is thermodynamically stable to room temperature, and/or Cr_2TiO_5, which is stable at high temperature but might be retained in metastable conditions to room temperature [28]. Nonetheless, data on wear resistance and tribological performances is not abundant. L.-M. Berger et al. reviewed the available literature [29], which suggests that Cr_2O_3-TiO_2 systems might not exhibit better sliding wear resistance than pure Cr_2O_3, at least at room temperature. This seems to be confirmed by the higher wear rates reported by L.-M. Berger et al. [30] and F.-L. Toma et al. [31] for Cr_2O_3-TiO_2 coatings in comparison to pure Cr_2O_3 ones under ball-on-disc test conditions. This might be related to the lower hardness of Cr_2O_3-TiO_2 coatings, which was independently verified for TiO_2 contents up to 25 wt.% [32] and 32 wt.% [33]. Further, Barbezat et al. reported that plasma sprayed Cr_2O_3 – 10, 20 and 30 wt.% TiO_2 exhibit slightly higher wear rates than pure Cr_2O_3 under abrasive pin-on-disc test conditions (coated pin sliding against a 150-mesh SiC abrasive paper) [19]. On the other hand, Vernhes et al. showed a more complex picture [14]. Whilst they confirmed that plasma sprayed Cr_2O_3 is more sliding wear resistant than Cr_2O_3-TiO_2 coatings (the composition of the latter has not been disclosed), they also found that one kind of Cr_2O_3-TiO_2 coating is superior to Cr_2O_3 under wet

and dry abrasion conditions. Hence, the Cr_2O_3-TiO_2 system deserves further investigations to clarify its potential.

Even fewer data is available concerning other, potentially interesting binary systems, such as Cr_2O_3-Al_2O_3 and Cr_2O_3-ZrO_2. Information on thermal spray coatings belonging to the latter system is practically inexistent but for a few studies on Cr_2O_3-ZrO_2-CaF_2 for high-temperature applications, which are not pertinent to the scope of the present work [34,35]. The Cr_2O_3-Al_2O_3 system has mostly been studied on the Al_2O_3-rich side, seeking to use Cr_2O_3 as a means to promote the nucleation of α-Al_2O_3 instead of γ-Al_2O_3 [36–39], an effort which seems to have been met with only partial success. However, not much is known on the performance of Al_2O_3-doped Cr_2O_3 [29]. It should develop a single-phase, hexagonal solid solution [37], due to the complete mutual solubility of Al_2O_3 and Cr_2O_3 at high temperatures [29], together with the fact that Cr_2O_3 (unlike Al_2O_3) never forms metastable phases, even when impact-quenched.

There is, therefore, a clear need to investigate the wear behaviour of Cr_2O_3-TiO_2, Cr_2O_3-Al_2O_3, Cr_2O_3-ZrO_2 alloys under various conditions, comparing them to pure Cr_2O_3, which is the goal of the present paper. Sliding and abrasive wear resistance have been specifically addressed through ball-on-disc tests against different counterparts and rubber-wheel tests against quartz particles. The structure and microstructure of the coatings have also been analysed as a basis to understand the wear mechanisms.

It should be mentioned that a very recent publication did examine the properties of plasma sprayed Cr_2O_3-Al_2O_3-TiO_2 coatings [40]. However, that paper dealt with coatings obtained from blends of pure Cr_2O_3, Al_2O_3 and TiO_2 powders. Apart from minor diffusion of low-melting TiO_2 within the Cr_2O_3 splats, no interaction occurred among powder particles during plasma-spray processing. Therefore, the coatings did not consist of “true” alloys. They were composites, made of the juxtaposition of distinct, single-oxide splats [40]. Their properties, including the resistance to sliding wear, were intermediate between those of the individual constituents.

The present work, by contrast, uses pre-alloyed feedstock powders, where each particle is made of two intimately mixed oxide constituents, either in the form of a solid solution, a binary compound, or tightly bound pure oxides. Plasma spray processing of those powders is therefore expected to promote even better homogenization. As the particles melt, they form a single-phase liquid, which is then impact-quenched; hence, segregation would be unlikely. The response of these “true” alloy coatings cannot be regarded as a linear combination of individual constituents.

2. Experimental

2.1. Feedstock powders

Six distinct feedstock powders were employed for the present study (Table 1). They were all chromium oxide-based, including pure Cr_2O_3 and Cr_2O_3 alloyed with TiO_2, Al_2O_3 and ZrO_2. Two main criteria guided the selection of the powders:

(1) Their particle size distributions had to be as close as possible, to avoid introducing an additional, confounding effect of size distribution on the properties of the resulting coatings. Differences among them must be essentially due to chemical composition alone.

(2) The constituents in binary systems must be intimately mixed, i.e. the powders must consist of a homogeneous solid solution or, at least, contain both oxide phases within each particle, to study the effect of alloyed (not composite) coatings.

Actual particle size distributions were verified in this work through laser diffraction analysis (Mastersizer 2000, Malvern Instruments, Malvern, UK, equipped with a Hydro-2000 S wet dispersion unit) and the results listed in Table 1 corroborate the assumption that size ranges are sufficiently similar as to avoid a major effect of this parameter on coating properties. Only minor discrepancies exist between nominal and measured size distributions, with the Cr_2O_3-10%ZrO_2 powder being finer than the others, whilst the pure Cr_2O_3 is slightly coarser.

Table 1: Nominal and measured characteristics of the feedstock powders employed in this work.

Designation	**Commercial name**	**Nominal composition (wt.%)**	**Nominal particle size range -d_{90}+d_{10} [μm]**	**Measured particle size distribution d_{10}/d_{50}/d_{90} [μm]**
#1	Amperit 704.1 [1]	Cr_2O_3	-45+22	21.7 / 34.3 / 53.5
#2	Amperit 712.074 [1]	Cr_2O_3-25%TiO_2	-45+15	18.7 / 31.5 / 51.6
#3	Ruby L TSP [2]	Cr_2O_3-Al_2O_3	N/A	20.5 / 29.5 / 42.4
#4	Ruby TSP [2]	Cr_2O_3-Al_2O_3	N/A	14.8 / 27.5 / 48.6
#5	Cr_2O_3/ZrO_2 90/10 [3]	Cr_2O_3-10%ZrO_2	-36+10	14.6 / 24.0 / 39.0
#6	Cr_2O_3/ZrO_2 80/20 [3]	Cr_2O_3-20%ZrO_2	-45+5	15.2 / 28.1 / 49.7

[1] Manufacturer: Höganäs - H.C. Starck, Laufenburg, Germany
[2] Manufacturer: Saint-Gobain Coating Solutions, Northampton, MA, USA
[3] Manufacturer: Ceram GmbH, Albbruck, Germany

Scanning electron microscopy (SEM) was employed to check the morphology of the powder particles and their cross-sectional microstructure. Morphological observations were carried out with a Quanta-200 SEM (FEI-ThermoFisher Scientific, Eindhoven, NL): a small amount of each powder was spread onto a bi-adhesive graphite disc for this purpose. Cross-sections were obtained by mixing the powders in a room-temperature setting epoxy resin, which was subsequently ground with SiC papers (from P400 to P2500 sizes) to expose the sections of the particles, and polished with a polycrystalline diamond suspension (3 μm average particle size) and a silica nanoparticles suspension (≈60 nm average size). Cross-sectional observations were performed using a Nova NanoSEM 450 microscope (FEI) equipped with a Si-drift Energy-Dispersive X-ray (EDX) detector (Quantax-200, Bruker, Billerica, MA, USA), with prior Au sputtering (≈10 nm) on the resins to provide sufficient electrical conductivity.

2.2. Coating deposition

Coatings were deposited by the APS technique using a PlasmaTechnik A-3000 S 4/2 system (Oerlikon Metco, Pfäffikon, Switzerland) equipped with a Saint Gobain ProPlasma torch (Saint-Gobain Coating Solution, Avignon, France). Substrates were 50x100 mm plates made by Fe37 mild steel.

The plates were welded on a support and sand blasted with abrasive alumina sand having 0.35 – 0.5 mm particle size up to an average roughness Ra ≈ 3.5 μm.

The plasma gun was controlled by a robotic arm programmed with a horizontal meandering pattern. Identical process parameters were employed for all feedstock powders, as listed in Table 2. The average voltage recorded as a result of the chosen parameters was in the 70 – 71 V range.

Table 2: Plasma spray parameters employed for all powders.

Injector Angle	90°
Spray distance [mm]	120
Step [mm]	4
Traverse speed [mm/s]	850
Current [A]	650
Argon flow rate [SLPM]	43
Hydrogen flow rate [SLPM]	11
Carrier gas (Ar) flow rate [SLPM]	3.3
Powder feeder disc rotation	15%

A disc-based volumetric powder feeder was employed. Its rotation speed was keep fixed for all powders to achieve similar volumetric feed rates, which were converted to mass feed rates by weighing the amount of each powder sprayed for 2 min (Table 3).

Table 3: average mass feed rates measured for each powder during the spray experiments.

Feedstock powder	**Measured average mass feed rate [g/min]**
Cr_2O_3	24
Cr_2O_3-25%TiO_2	23
Cr_2O_3-Al_2O_3	19
Cr_2O_3-Al_2O_3	16
Cr_2O_3-10%ZrO_2	21
Cr_2O_3-20%ZrO_2	23

In the choice of process parameters, two different strategies were possible. On the one hand, each powder, as a function of its exact size distribution, density and melting range, might require slightly different torch settings to provide “optimal” coatings. However, this strategy would have implied some notable drawbacks, too. The concept itself of “optimal” is not univocally defined. Different optimization targets might be set: for example, maximizing deposition efficiency, hardness, or cohesive/adhesive strength; or minimizing porosity; or a combination thereof. On the other hand, changing the process parameters for each powder would have introduced a rather uncontrolled, confounding factor influencing the results. Therefore, to ensure that the differences among the

various coatings depend on chemical compositions only, identical process parameters were employed for all powders, which were chosen based on prior experience. It should be noted that the similarity among the particle size distributions means the "optimal" parameter settings for the various feedstock powders (however defined) would not differ much from one another. Though the plasma spray process is sensitive to process parameters, it is not exceedingly sensitive to small changes, so the coatings which would be obtained from individualized "optimal" settings would not have differed much from the one shown in this study.

Deposition Efficiency (DE) has been estimated considering the mass effectively deposited on the substrate through eq. (1):

$$DE = \frac{mass\ of\ coating}{sprayed\ mass} \cdot 100 = \frac{V \cdot \rho}{\dot{m} \cdot n \cdot \left(\frac{L}{v}\right) \cdot \left(\frac{l}{d}\right)} \cdot 100 \quad (1)$$

Where: V = volume of coating, $\dot{m}$ = powder feed rate, n = number of passes, L = length of the substrate, v = traverse speed, l = width of the substrate, d = pitch distance and ρ = density (assuming ρ-Al_2O_3=3.987 g/cm^3 [41], ρ-TiO_2=4.23 g/cm^3 [42], ρ-ZrO_2=5.68 g/cm^3 [43])

The overall number of torch cycles in front of the substrates was adjusted to achieve a target thickness of 250 – 300 µm, which was checked during the spray sessions using an electromagnetic induction gauge (Elcometer 300, Elcometer, Manchester, UK).

Moreover, during the spray sessions, a thermal camera imager (Ti300, Fluke, Norwich, UK) was directed to the samples in order to monitor the temperature, which was always kept around 100 °C by interrupting the deposition process for the necessary duration.

2.3. Characterization of the structure and microstructure of coatings

The phase composition of the coated samples was assessed by XRD, using the same conditions as for the feedstock powders (Section 2.1).

Coated samples were cut using automatic or semi-automatic metallographic cutting machines to preserve the coating integrity. Cross-sections were cold mounted in epoxy resin, cured at room temperature, then ground by SiC abrasive papers from P220 to P1200 size and polished through diamond pastes from 9 μm to 0.25 μm average size.

Coating thickness was evaluated by optical microscopy (ZeissAxio Observer, Carl Zeiss Microscopy GmbH, Jena, Germany), the results are an average of four measurements took in different areas of each coating. Porosity values were estimated by digital images analysis, again performed on optical microscopy images taken at 200× magnification. The results are an average of four measurements on the same sample, carried out through the ImageJ analysis software.

Additional observations of the coatings' cross-sectional microstructures were performed by SEM + EDX (Nova NanoSEM 450 with Quantax-200 EDX detector). Resin-mounted samples polished as described above were Au-sputtered as mentioned in Section 2.1 to ensure sufficient electrical conductivity of the whole surface.

Depth-sensing Vickers micro-indentation (Micro-Combi Tester) was also performed on the same polished cross-sections of the coatings, using an indentation load of 3 N (≈300 gf) with loading/unloading rates of 6 N/min and 15 s holding time at maximum load. Tests were conducted in accordance with the ISO 14577 standard (parts 1 to 4). Indentation hardness (properly designated as H_{IT} 3/30/15/30, hereafter H_{IT}) and indentation modulus (properly designated as E_{IT} 3/30/15/30, hereafter E_{IT}) were calculated. Results were the average of at least 20 indentations on each sample.

Scratch tests (Micro-Combi Tester) were performed on polished top surfaces, prepared as described later in Section 2.4 for sliding wear testing. Tests were carried out with a Rockwell-C type conical diamond tip (120° opening) having a rounded end with 200 μm radius. Preliminary tests were carried out in progressive loading mode by sliding once the indenter over the sample surface with linearly increasing load (0.1 – 30 N). Slight damage, in the form of microcracking and chipping of the surface, started in all cases at loads of about 20 – 22 N. Therefore, a constant load of 24 N was chosen for multipass scratch tests, which were performed by sliding the indenter 4 times over the

same track (always in the same direction). This simulates a repeated contact with a hard, abrasive asperity. The chosen load setting implies that some damage is produced at every pass, but it is not severe enough to cause complete disruption already during the first cycle. As a result, the multipass test allows to check for damage accumulation effects. In all cases, the scratch length was 6 mm and the speed was 1 mm/min. Three progressive-load and three constant-load multipass tracks were performed on each sample. Scratch tracks were inspected by optical microscopy and SEM (Nova NanoSEM 450).

2.4. Dry sliding wear testing

Dry sliding wear tests were performed in ball-on-disc configuration at room temperature with a THT tribometer (Anton Paar TriTec) according to the ASTM G99 standard, using two distinct types of spherical counterparts: sintered alumina (nominal hardness: ≈19 GPa) and yttria-stabilized zirconia (5.7±0.2 wt.% Y_2O_3; hardness: 1232±33 $HV_{0.3}$), both with 6 mm diameter.

The specimens were surface polished using a diamond grinding disc (P220), a diamond pad with 9 μm-size polycrystalline diamond slurry, a polishing cloth with 3 μm-size polycrystalline diamond slurry, and a cloth with colloidal silica suspension (≈60 nm particle size) to achieve a mirror-like finish ($Sa < 0.1$ μm) and eliminate any confounding effect due to the surface roughness of as-deposited coatings on the friction and wear behaviour.

During each test, the friction coefficient was measured by the instrument though a load cell attached to the ball-holding arm. The wear rate of the ball was determined from the worn diameter with an optical microscope. The wear rate of the sample was evaluated by measuring the volume loss on the wear track by a structured illumination profilometer (ConfoSurf, Confovis GmbH, Jena, Germany) attached to a Nikon Eclipse LV150N optical microscope.

The surfaces and polished cross-sections of worn samples were further observed by SEM + EDX (Nova NanoSEM 450 + Quantax-200). Cross-sections were obtained by metallographic cutting,

cold-mounting in epoxy resin, grinding with SiC papers (from P400 to P2500) and polishing with 3 μm-size polycrystalline diamond slurry and colloidal silica suspension (≈60 nm particle size).

Worn surfaces and loose debris collected on the surface of the tested samples outside the wear track were further analysed by micro-Raman spectroscopy (LabRam, Horiba Jobin-Yvon, Longjumeau, France) using a 532 nm-wavelength excitation source focused through a 100× microscope objective.

Some of the debris was also collected onto Cu-based grids and observed by transmission electron microscopy (TEM: Talos F200S G2, Thermo Fisher Scientific).

2.5. Dry sand abrasion testing

Wear behaviour was evaluated by using a modified version of ASTM G65 abrasion test standard. The procedure is the same as originally described by the authors in [44] and subsequent publications. Briefly, an equipment with 5 distinct test positions was employed, whereby each sample was cycled between positions every 12 min, until all samples have been tested in all locations for a total duration of 60 min, to eliminate any influence from inter-location variability. Further, coatings having different compositions were run together during each testing session, to avoid any systematic error between measures.

Samples were weighed before testing and during each position change (i.e. every 12 min) with a ±0.1 mg balance.

Test conditions included a normal load of 23 N, a peripheral velocity of 1.64 m/s on the wheel surface, a total relative distance of 5904 m; SiO_2 (quartz) was used as the abrasive (0.1 – 0.6 mm particle size range) at a flow rate of 25 g/min.

3. Results

3.1. Microstructure of powders and coatings

The cross-sectional microstructures of the mixed-oxide powders (Figure 1D,G,J,M,P) confirms that none is a simple blend of distinct phases. The Cr_2O_3-25%TiO_2 (Figure 1D) particles consist of a homogeneous solid solution, with some needle-like secondary phases as seen in the inset micrograph. The two Cr_2O_3-Al_2O_3 (Ruby-L, Ruby-S) powders (Figure 1G,J) also consist of solid solutions, though differences in backscattered electron contrast levels show some particle-to-particle variability in chemical composition. Especially in the Ruby-S powder, bright particles (Figure 1J – label 1) rich in Cr co-exist with increasingly dark ones (labels 2, 3) containing higher relative amounts of Al. The Ruby-L powder is more homogeneous, despite occasional dark, Al-rich particles (Figure 1G, see arrow). The Cr_2O_3-ZrO_2 powders (Figure 1M,P) show comparatively more compositional variability, both among distinct particles and within each particle. Dark, Cr_2O_3-rich areas and bright, ZrO_2-rich areas are recognizable. However, also in this case, few areas consist only of completely pure Cr_2O_3 or completely pure ZrO_2.

The chemical composition of the powders, obtained by EDX scans performed over areas imaged at 400× on the polished cross-sections, is listed in Table 4. Very good agreement between nominal and actual compositions is found for the Cr_2O_3-25%TiO_2, Cr_2O_3-10%ZrO_2 and Cr_2O_3-20%ZrO_2 powders, though some of them also contain a little SiO_2. Among the Cr_2O_3-Al_2O_3 (“Ruby”) powders, the nominal composition of which was not disclosed, it is found that Ruby-S is much richer in Al_2O_3 (on average) than Ruby-L.

A more detailed discussion on the microstructure of the powders, including their phase composition and additional EDX analyses to corroborate the chemical composition, can be found in the Supplementary Material, section S1. The Supplementary Material also discusses the occasional presence of bright inclusions in the pure Cr_2O_3 powder, which likely consist of metallic Cr.

Table 4: Chemical composition of the feedstock powders (average ± standard deviation) as measured by EDX analyses on large-area scans, expressed in wt.% of stoichiometric oxide compounds. In every case, the amount of Cr_2O_3 is the balance to 100%.

Powder	**Measured composition (wt.%)**
Cr_2O_3-25%TiO_2	TiO_2: 26.5±0.5
	SiO_2: 1.7±1.3
Ruby L	Al_2O_3: 15.7±0.2
Ruby S	Al_2O_3: 35.4±0.1
Cr_2O_3-10%ZrO_2	ZrO_2: 10.7±0.8
Cr_2O_3-20%ZrO_2	ZrO_2: 20.0±1.2
	SiO_2: 2.3±0.4

Table 5: Thickness and porosity of the plasma-sprayed coatings. Average ± standard deviation.

	Thickness [µm]	**Porosity [%]**
Cr_2O_3	253±3	7.7±0.9
Cr_2O_3-25%TiO_2	264±5	6.8±1.4
Ruby-L	251±4	8.8±0.6
Ruby-S	281±8	7.7±0.6
Cr_2O_3-10%ZrO_2	291±2	8.7±1.0
Cr_2O_3-20%ZrO_2	272±4	6.9±1.7

Powder particles' morphologies can be told into two types. The dense, angular particles of the pure Cr_2O_3 (Figure 1A), e Cr_2O_3-25%TiO_2 (Figure 1D), Cr_2O_3-10%ZrO_2 (Figure 1J) and Cr_2O_3-20%ZrO_2 (Figure 1M) powders are typical of a fusing-and-crushing manufacturing method. The Ruby-L and Ruby-S powders (Figure 1G,J) consist of rounded and somewhat porous aggregates of fine, faceted grains, indicating an agglomeration and sintering process.

Regardless of this difference in powders' morphology, microstructurally similar coatings were obtained. All their thickness values (Table 5) are within the desired range of 250 – 300 µm (Section 2.2), and porosity values are practically indistinguishable, given the associated error ranges (Table 5; also see their overviews from optical micrographs in the Supplementary Material, section S2). There are no major defects either in the coatings or along the interface with the substrate, and no notable inter-layer defects.

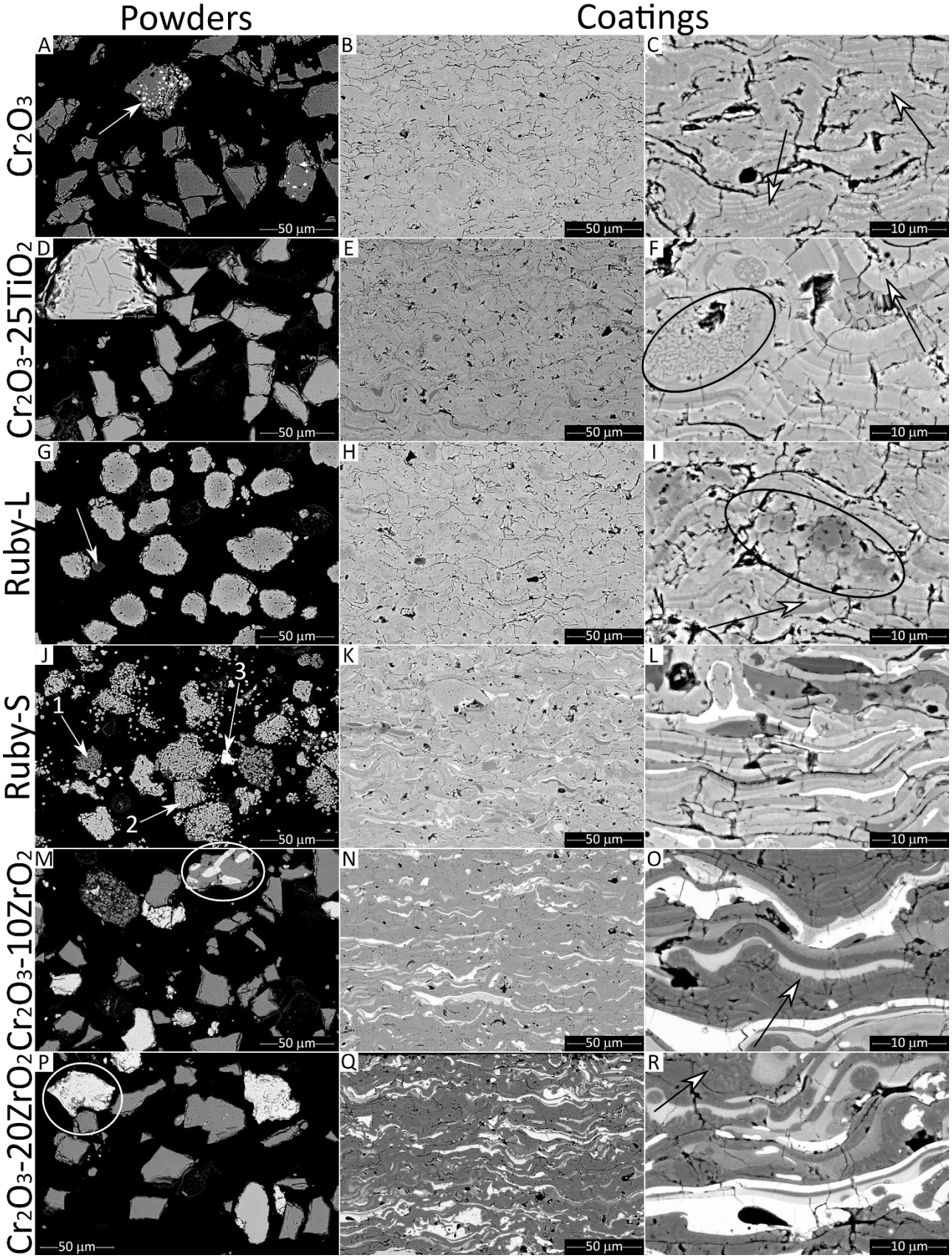

Figure 1: Cross-sections of spray powders (A,D,G,J,M,P), coatings' overviews (B,E,H,K,N,Q) and details (C,F,I,L,O,R): backscattered electron SEM micrographs. Cr_2O_3 (A-C), Cr_2O_3-25%TiO_2 (D-F), Ruby-L (G-I), Ruby-S (J-L), Cr_2O_3-10%ZrO_2 (M-O), Cr_2O_3-20%ZrO_2 (P-R).

Looking at the coatings in greater detail (Figure 1C,F,I,L,O,R), their porosity consists of inter- and intra-lamellar microcracks; irregularly shaped pores, due to imperfect stacking between adjacent lamellae; and rounded pores, due to gas entrainment within the molten material. All of these features are typical of plasma sprayed ceramics [16,45–48]. Rounded inclusions, such as are shown in the circled areas of Figure 1F,I, consist of partially unmelted particles.

In terms of compositional homogeneity, each coating tends to reflect the characteristics of the corresponding feedstock powder (Figure 1). Long-range diffusion is, indeed, not permitted during plasma spraying, due to high cooling rates. Therefore, the composition of individual powder particles directly translates into the composition of individual splats, as anticipated in the Introduction. Thus, the Cr_2O_3-Al_2O_3 coating (Figure 1H,I) obtained from the Ruby-L powder exhibits less variability in backscattered electrons contrast among distinct lamellae than does the coating from the Ruby-S powder (Figure 1K,L).

The Cr_2O_3-ZrO_2 coatings exhibit an even wider range of backscattered electron contrast levels in distinct lamellae (Figure 1N,O,Q,R). However, the intra-particle inhomogeneity that existed within individual particles is no more present in the coatings. The compositionally distinct areas, which were originally distinguishable in the particles, were mixed thoroughly when the latter were melted during spraying. Overall, the formation of alloyed coatings can be confirmed.

Details of the microstructure and phase composition of the coatings, including a discussion on the phase evolution during spraying and on the deposition efficiency, is provided in the Supplementary Material, Section S2.

3.2. Depth-sensing indentation testing

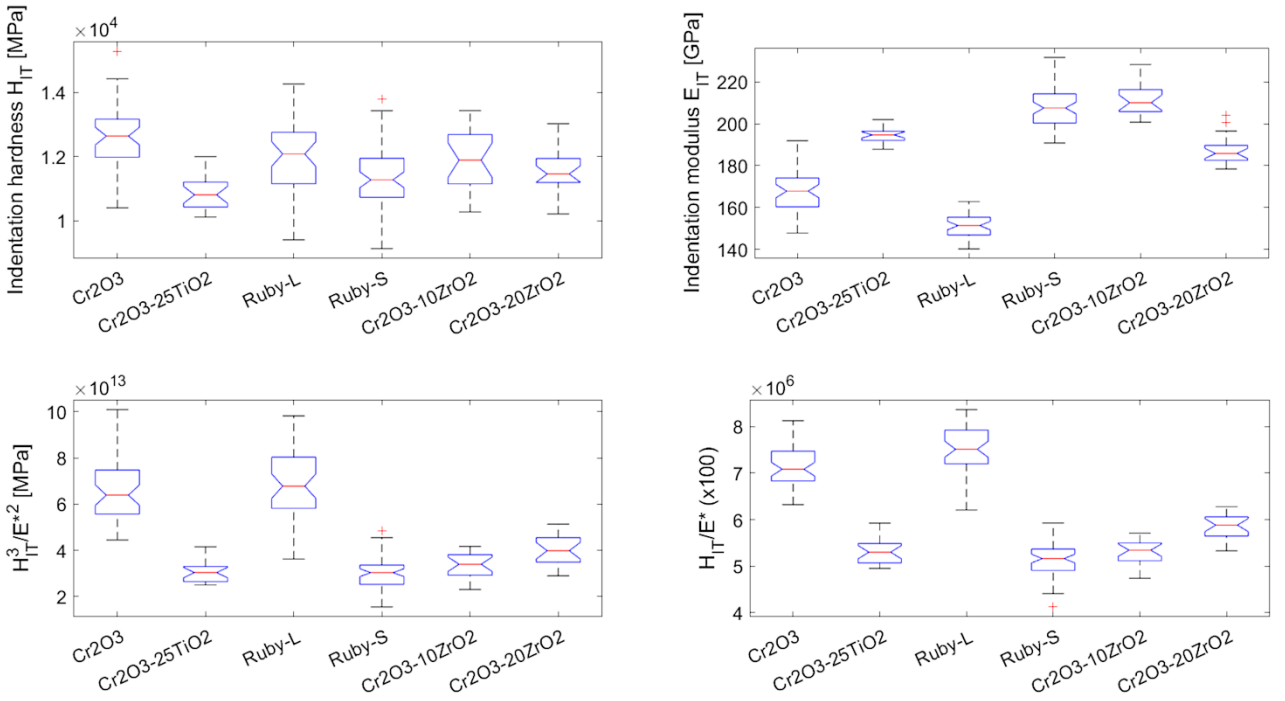

Figure 2: Boxplots showing the results of depth-sensing Vickers micro-indentation experiments: indentation hardness (H_{IT}), indentation modulus (E_{IT}), and the ratios H_{IT}/E^* and H_{IT}^3/E^{*2} between indentation hardness and plane-strain modulus $E^* = E_{IT}/(1-\nu^2)$. Notches represent the 95% confidence intervals, dashed lines represent the entire data range except outliers (crosses), horizontal red and blue lines represent the median and the 1st and 3rd quartile.

The coatings differ significantly from one another in terms of both hardness (H_{IT}) and elastic modulus (E_{IT}), as can be seen from the corresponding boxplots in Figure 2. Especially by comparing the 95% confidence intervals, graphically represented by the notches, it is seen that pure Cr_2O_3 is the hardest of all coatings. All alloying additions have the effect of reducing it to various extents: from a lesser decrease in case of Ruby-L, to a quite large drop for Cr_2O_3-25%TiO_2. The hardest coatings, i.e. Cr_2O_3 and Ruby-L, are also those possessing the lowest elastic modulus. As a result, the parameters H_{IT}/E^* and H_{IT}^3/E^{*2} vary widely from rather large values for these two samples to lesser (and more similar) values for all others. Further statistical analyses are provided in the Supplementary Material, section S3.

3.3. Single-asperity contact response: simulation through scratch testing

For all coatings, the average penetration depth of the indenter during each of the 4 scratch passes is almost always comprised between 4 μm and 8 μm. Namely, it is not possible to differentiate among the coatings based on indenter penetration depth in scratch tests. This finding seems to contradict the differences in hardness among the various coatings (Section 3.2).

SEM observation of scratch tracks (Figure 3) readily clarifies that brittle fracture dominates the behaviour of the coatings upon repeated scratching and, most importantly, that there are conspicuous differences among the samples in terms of failure severity. Failure was more extensive in the Cr_2O_3 (Figure 3A) and Cr_2O_3-Al_2O_3 (Ruby-L, Figure 3C, and Ruby-S, Figure 3D) coatings: larger areas of material are uplifted and removed from the multipass tracks (see circled areas). Conversely, the Cr_2O_3-25%TiO_2 (Figure 3B), Cr_2O_3-10%ZrO_2 (Figure 3E) and Cr_2O_3-20%ZrO_2 (Figure 3F) coatings exhibit less failure.

The exact mechanisms for brittle failure during scratch testing are clarified by detailed SEM observations. The single-pass scratch tracks, imaged in the area where the applied load was 24 N, highlight the earliest stages of failure. Figure 5A shows the case for pure Cr_2O_3, but similar observations were made in every case. Failure begins through the formation of small cracks and/or opening of pre-existing cracks. Both interlamellar and intergranular cracks are observed. Interlamellar cracks proceed along the boundary between adjacent lamellae (Figure 5A: label 2); intergranular cracks occur between adjacent grains inside a lamella (Figure 5A: label 1).

Both types of cracks extend conspicuously after repeated scratching. Figure 5B shows extensive intergranular failure on the Cr_2O_3 coating after a multipass test. Figure 5C shows an uplifted portion of material on the surface of the same coating: lamellae were detached from one another through the progression of interlamellar cracks (label 2) and were fragmented through intergranular cracks (label 1). The latter type of cracks also highlights the typical columnar microstructure within each splat.

Failure modes are qualitatively the same in all coatings: for instance, Cr_2O_3-ZrO_2 coatings also show extensive intergranular failure (Figure 5D,E) and material uplifting (Figure 5F) through intergranular (label 1) and interlamellar (label 2) cracks. Differences reside in the extent to which damage progresses in different coatings.

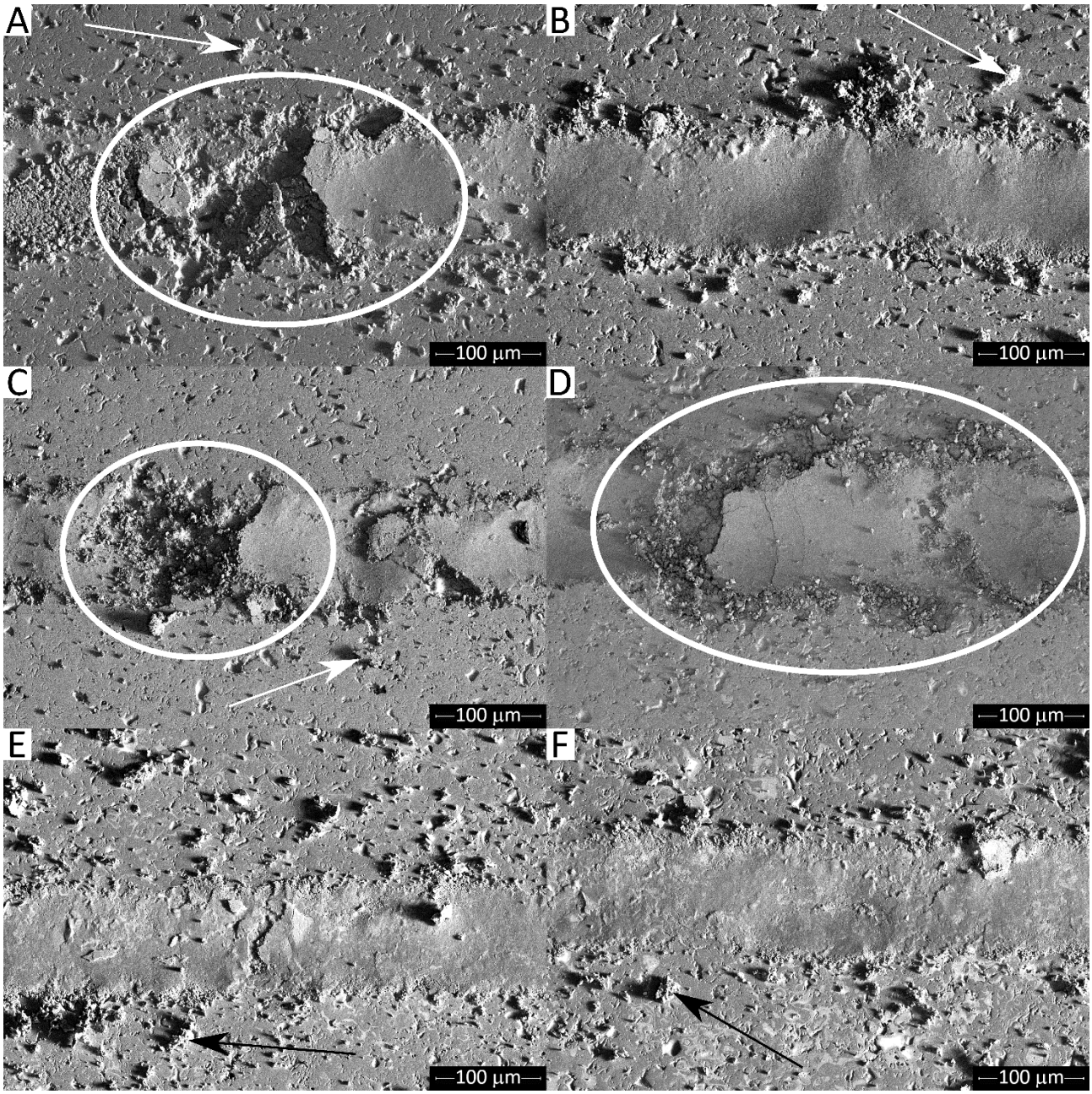

Figure 3: SEM micrographs of multipass scratch tracks on plasma sprayed coatings: Cr_2O_3 (A), Cr_2O_3-25%TiO_2 (B), Ruby-L (C), Ruby-S (D), Cr_2O_3-10%ZrO_2 (E), Cr_2O_3-20%ZrO_2 (F).

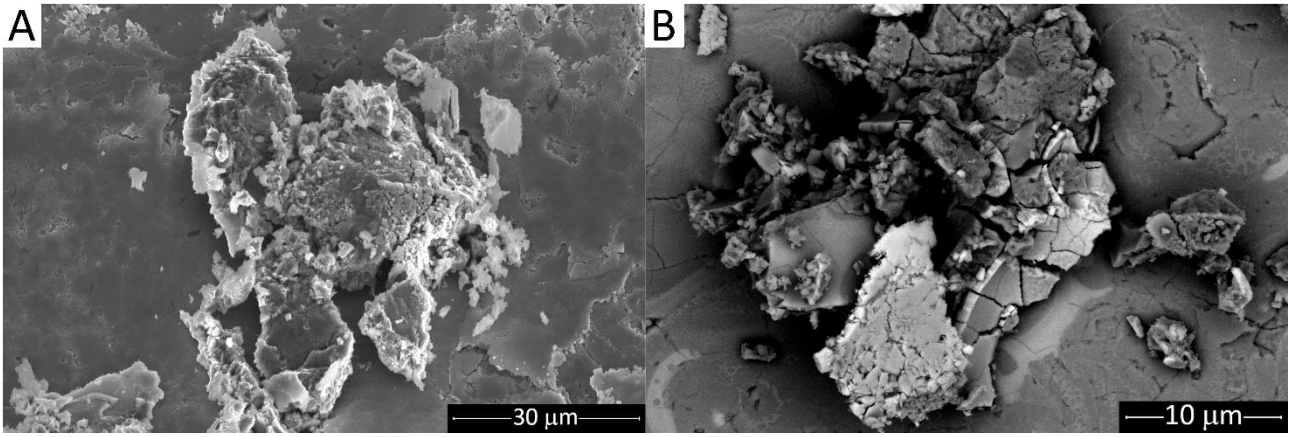

Figure 4: SEM micrographs showing details of debris particles scattered on the coating surfaces after multipass scratch testing: Cr_2O_3-25%TiO_2 (A) and Cr_2O_3-10%ZrO_2 (B).

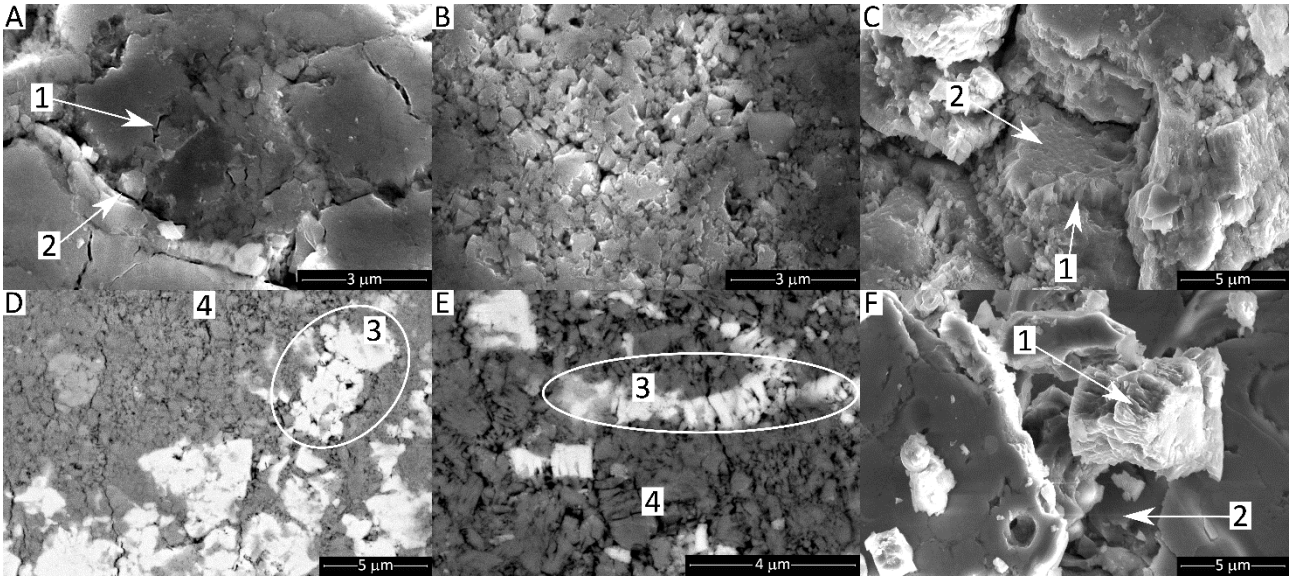

Figure 5: backscattered electrons SEM micrographs showing details of scratch tracks: progressive single-pass track on plasma sprayed Cr_2O_3 in the 24 N-load area (A), and multipass tracks on Cr_2O_3 (B,C) Cr_2O_3-10%ZrO_2 (D), Cr_2O_3-20%ZrO_2 (E,F) coatings.

In the Cr_2O_3-ZrO_2 coatings intergranular fracture seems to affect Cr_2O_3-rich areas (Figure 5D,E: label 4) more severely than ZrO_2-based areas (Figure 5D,E: label 3). It would therefore look like ZrO_2-based areas do exert a toughening action. The Supplementary Material, section S2, shows that ZrO_2-based areas consist mainly of the cubic phase, which should not exhibit the same toughening mechanisms as are usually known for the tetragonal phase. Various Raman spectra (Figure 6) acquired on ZrO_2-based lamellae inside and outside a single-pass scratch track (in the 24 N-load area) accordingly do not show any perceivable phase transition. Cubic zirconia is the only

detectable phase. Hence, transformation toughening is not taking place in this case, yet even cubic ZrO_2 seems to be tougher than Cr_2O_3-based areas.

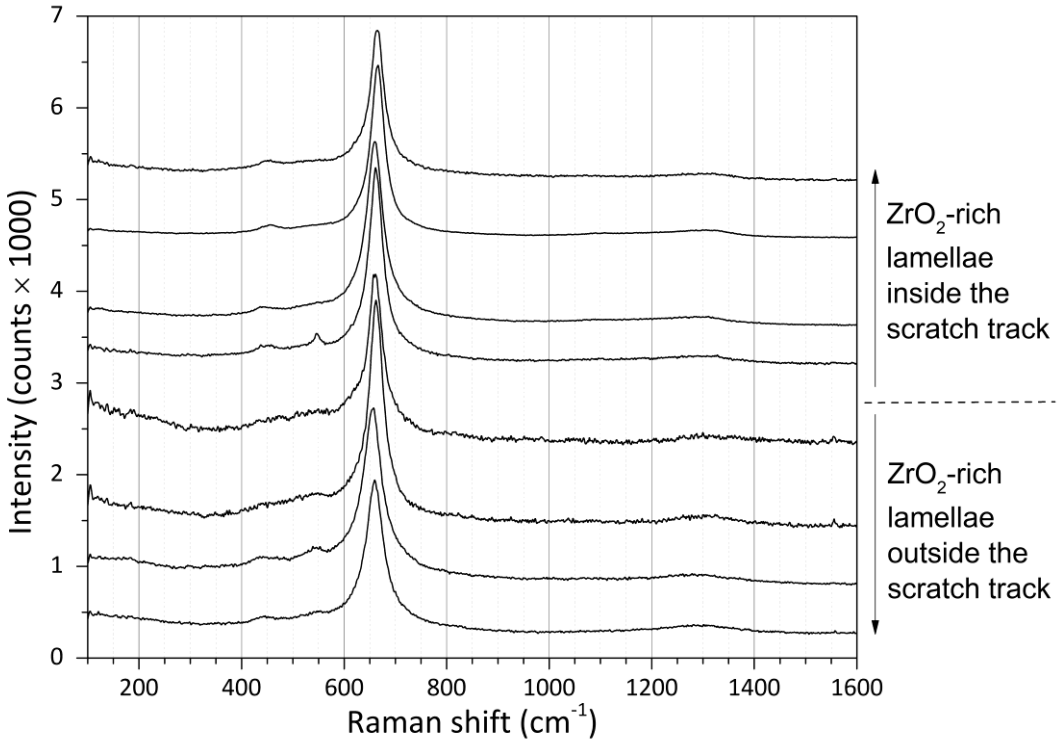

Figure 6: Raman spectra acquired on various lamellae on the surface of the Cr_2O_3-20%ZrO_2 coating, inside and outside the single-pass scratch track.

3.4. Wear behaviour under sliding and abrasive conditions

3.4.1. Analysis of wear rates

A comparison between the specific wear rates observed after the various sliding and abrasive wear tests (Figure 7A) highlights some very interesting trends. Abrasive wear rates are more severe than sliding ones; indeed, all abrasive wear rates are $\geq 3\times10^{-4}$ $mm^3/(N\cdot m)$ whereas dry sliding wear rates are $<10^{-4}$ $mm^3/(N\cdot m)$ except for the Cr_2O_3-25%TiO_2 coating, whose sliding wear rates are $\approx 1.5\times10^{-4}$ $mm^3/(N\cdot m)$. Most remarkably, the ranking among the coatings is almost the opposite under sliding or abrasive wear conditions.

Against both Al_2O_3 and ZrO_2 counterparts (Figure 7A), the ranking of the coatings in order of increasing sliding wear rates (decreasing sliding wear resistance) is Cr_2O_3 < Ruby-L < Ruby-S ≈

Cr_2O_3-10%ZrO_2 < Cr_2O_3-20%ZrO_2 < Cr_2O_3-25%TiO_2. The excellent sliding wear resistance of plasma sprayed pure Cr_2O_3 has long been known [15]. The higher sliding wear rate of Cr_2O_3-25%TiO_2 coatings compared to pure Cr_2O_3 at room temperature has also been observed in the few extant studies on similar systems [14,30,33], as anticipated in the Introduction. Toma et al. also reported higher sliding wear rates of Cr_2O_3-15%TiO_2 coatings compared to pure Cr_2O_3 under reciprocating sliding conditions against an Al_2O_3 counterpart [31].

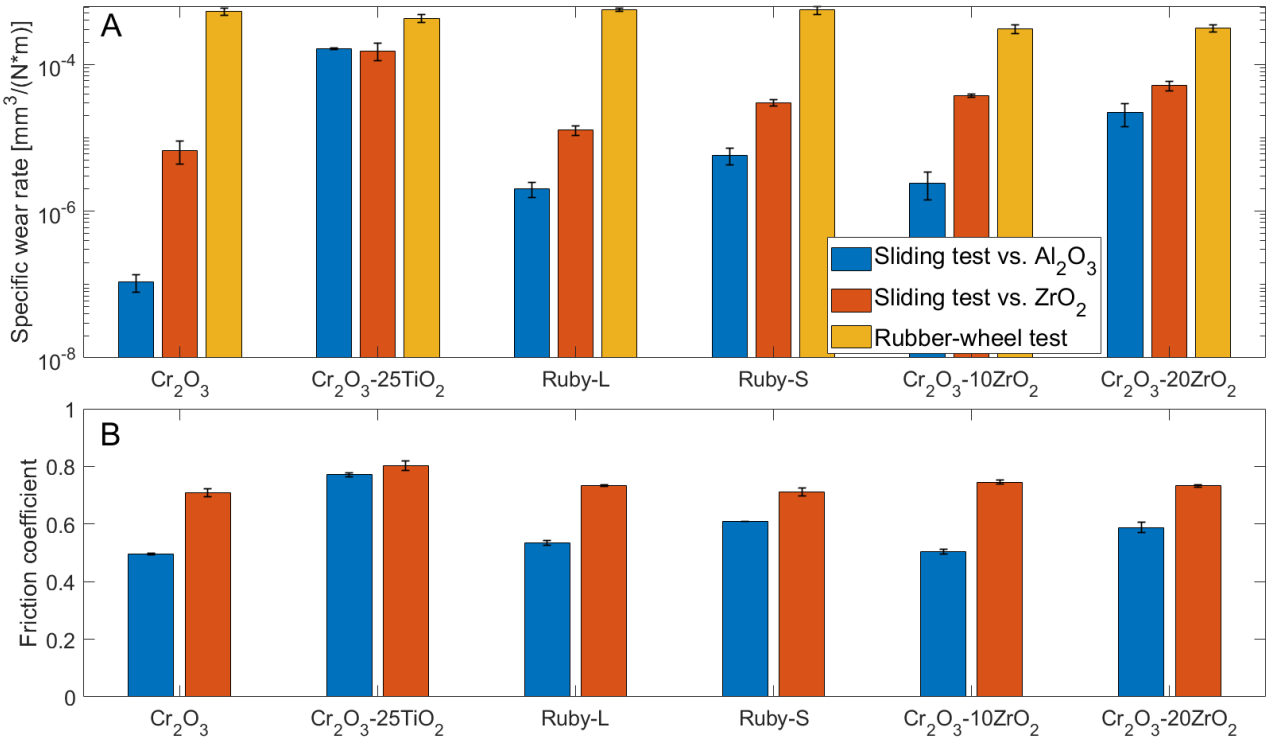

Figure 7: specific wear rates measured on all coatings after sliding wear tests against Al_2O_3 and ZrO_2 balls and after dry sand-rubber wheel abrasive wear test (A), and average steady-state friction coefficients measured in the sliding wear tests (B).

Though the ranking in terms of wear rates is basically the same in tests against both Al_2O_3 and ZrO_2 balls, values tend to increase in the latter case (Figure 7B), and the increase is proportionally greater for the most wear-resistant samples. As a result, coatings' performances are more levelled against ZrO_2 than they are against Al_2O_3. Namely, although the specific wear rates of pure Cr_2O_3 are the lowest against both counterparts, the wear rate against ZrO_2 is 60 times higher than it is against Al_2O_3. The increase in specific wear rate when changing from Al_2O_3 to ZrO_2 counterpart is

progressively smaller for the Ruby-L, Ruby-S, Cr_2O_3-10%ZrO_2 and Cr_2O_3-20%ZrO_2 coatings: in the latter case, it is only 2.4 times higher against ZrO_2 than it is against Al_2O_3. Cr_2O_3-25%TiO_2 suffers the most severe wear rate, but its value is approximately the same against both ZrO_2 and Al_2O_3.

It is further observed that the sliding wear response does not seem to be affected by chemical affinity between the coatings and the counterparts. Namely, in the case of ductile materials (e.g. metals), is well known that self-mating couplings are often inadvisable, because they can trigger severe adhesive wear due to chemical affinity [49]. Had the same been true for the present samples, sliding against either Al_2O_3 or ZrO_2 counterparts should have respectively put the Ruby or Cr_2O_3-ZrO_2 coatings at an especial disadvantage, due to greater chemical affinity. This, however, seems not to be the case. Against the Al_2O_3 counterpart, the Ruby-L coating wears down less than do the Cr_2O_3-ZrO_2 coatings, despite the compositional affinity. Its wear rate also increases proportionally more than that of the Cr_2O_3-ZrO_2 coatings when changing to a ZrO_2 counterpart, which is the opposite of what would be expected, had chemical affinity been relevant to the tribological results. Further, the friction coefficient against each counterpart seems to be mostly independent of the coating material. Except for the Cr_2O_3-25%TiO_2 coating, all other samples exhibit average steady-state friction coefficient (i.e. excluding the initial run-in stage) of 0.5 – 0.6 against Al_2O_3 and 0.7 against ZrO_2, which means there is no specific adhesion effect in contacts between chemically similar materials.

Under abrasive conditions, by contrast, the Cr_2O_3 and Cr_2O_3-Al_2O_3 (Ruby-L and Ruby-S) coatings exhibit the highest wear rates. Cr_2O_3-25%TiO_2 has somewhat lower abrasive wear rates, which was also reported in [14], although that finding pertained to a coating obtained from a nanostructured feedstock, different from the present one. The Cr_2O_3-ZrO_2 coatings have the lowest abrasive wear rates.

The sliding wear resistance of the coatings against both counterparts tends to rank according to their hardness (Figure 2). Cr_2O_3 and Ruby-L are indeed the hardest among the samples; Ruby-S, Cr_2O_3-10%ZrO_2 and Cr_2O_3-20%ZrO_2 have intermediate hardness (with Cr_2O_3-10%ZrO_2 being harder than Cr_2O_3-20%ZrO_2); Cr_2O_3-25%TiO_2 is the softest one and indeed suffers by far the highest sliding wear rates. The most sliding wear resistant coatings are also those with the highest H_{IT}/E^* and H_{IT}^3/E^{*2} ratios. The abrasive wear resistance, to the contrary, ranks according to the extent of damage observed after multipass scratch testing (Section 3.3).

To corroborate these considerations, the principal component analysis (PCA) [50] was performed to check for linear correlations between mechanical properties and specific wear rates under sliding and abrasive wear conditions. PCA is a dimensionality reduction technique whereby a dataset consisting of measurements of *n* different properties is linearly transformed into a new set of variables, the principal components, computed in such a way that the first component explains the maximum possible amount of the overall variance of the dataset, and every subsequent component explains the maximum fraction of the residual variance. The principal components have no physical meaning per se, but through their use it is possible to describe most of the variance in the system by focusing solely on the first two or three components. The problem is thus reduced to a 2- or 3-dimensional system, amenable of graphical representation, with minimal loss of information. By plotting as vectors the contributions of each original variable to the chosen components, it is possible to determine which variables have close linear correlations (parallel/antiparallel vectors) and which are linearly unrelated (orthogonal vectors). This technique has already been employed by the authors to study the correlations between properties and tribological performances of thermal spray coatings [51,52]. The reader is directed to these references for a summary description of the PCA method. Its implementation in MATLAB R2018b was employed here.

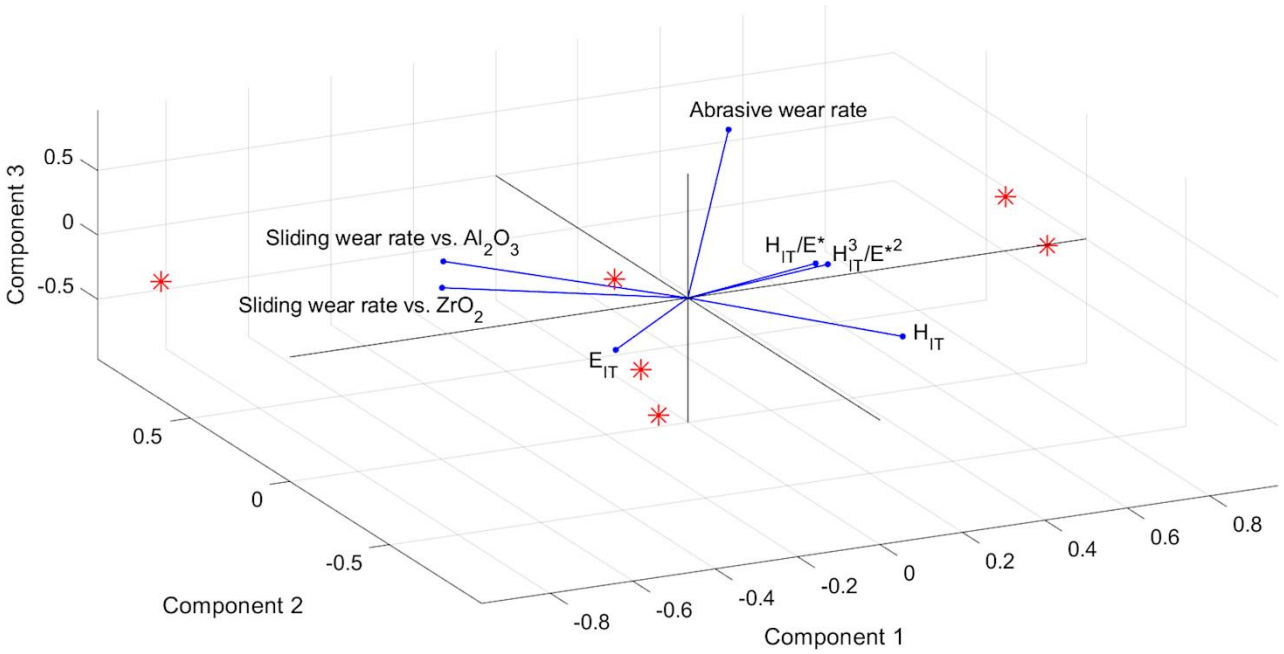

Figure 8: results of the principal component analysis correlating wear rates to micromechanical properties. Blue vectors represent the contributions of each property to the first three principal components; red asterisks represent the coordinates of coating in the new space of the principal components.

Specifically, the first three principal components explain almost 98% of the overall variance of the current dataset. The corresponding plot (Figure 8) shows that the vectors representing the sliding wear rates of the coatings tested against Al_2O_3 and ZrO_2 counterparts are antiparallel to the hardness vector, implying a close correlation (wear rates decrease as hardness increases), confirming the previous qualitative observations. The H_{IT}/E^* and H_{IT}^3/E^{*2} ratios are somewhat less closely correlated to sliding wear rates, compared to hardness alone. The vector representing the abrasive wear rate, on the other hand, is almost perpendicular to all others, which means it does not correlate well with either the sliding wear rates or all micro-mechanical properties quantified by depth-sensing micro-indentation. This corroborates the previous observation that abrasive wear resistance correlates well only with the qualitative results of scratch tests.

3.4.2. Identification of wear mechanisms: sliding wear tests against Al_2O_3 ball

Under sliding wear conditions against an Al_2O_3 counterpart, wear is associated with localized spallation of the coating surface (Figure 9A,C,E,G,I,K: some spalled areas are circled). Detailed

views show that spallation is due to the detachment of lamellae (Figure 9B,D,F,H,J,L). Indeed, the gently curved shape of individual lamellae, or fragments thereof, can be recognized in the SEM micrographs, implying that the lamellae directly above them were detached along the boundary and removed.

Cross-sectional views consistently highlight the formation of microcracks along the lamellar boundary, or the propagation of pre-existing interlamellar defects (Figure 10: some of those interlamellar cracks are marked by arrows). Cracks only occur in the immediate vicinity of the outer surface, without affecting deeper areas, and their lateral extension covers one or two lamellae at the most. More severe wear is therefore associated with more frequent occurrence of lamellar spallation.

These mechanisms seem to straddle the edge between the two main wear regimes of ceramics as they have been described in [53,54]: mild wear, with minimal loss and smooth surfaces, and severe wear, involving brittle fracture and surface roughening. A specific wear rate of $\approx 10^{-6}$ $mm^3/(N \cdot m)$ is regarded as the threshold between these two regimes [53,54]. Pure Cr_2O_3, with its very smooth surface, where brittle detachment of lamellae is restrained to a minimum, accordingly exhibits a specific wear rate below the threshold against the Al_2O_3 counterpart (Figure 7A). When coatings exhibit a mix of smooth areas and roughened pits, the wear rate raises slightly above the 10^{-6} $mm^3/(N \cdot m)$ threshold. The Cr_2O_3-TiO_2 coating, with a wear rate well above the threshold, exhibits an extensively roughened surface.

With specific regard to plasma sprayed Cr_2O_3, Kitsunai et al. [55] distinguished mild wear, in the form of "ploughing and powder formation", and two severe wear modes: crack and powder formation, and flake formation. The latter are characterized by increasing degree of wear severity and differ in the extension of cracks (note that similar regimes are also found for bulk ceramics [56]). Based on this classification, Cr_2O_3 can be regarded as being in the ploughing wear regime under the present conditions, whilst the addition of alloying elements shifts the samples (to different extents) towards a crack and powder formation regime. Flake formation never occurs under the

present conditions, as it would imply crack propagation over a wider range than it is seen in Figure 10. This assignment can be tested against the typical ranges of the dimensionless wear coefficient (K_{ad}) for each regime, which are given as $\leq 10^{-4}$, $\sim 10^{-3}$, $10^{-2} - 10^{-1}$, respectively [55]. Since $K_{ad} = K \times H$, the dimensionless wear coefficients of the present samples are computed as 1.4×10^{-6}, 1.8×10^{-3}, 2.4×10^{-5}, 6.5×10^{-5}, 2.9×10^{-5}, 2.5×10^{-4} for pure Cr_2O_3, Cr_2O_3-25%TiO_2, Ruby-L, Ruby-S, Cr_2O_3-10%ZrO_2 and Cr_2O_3-20%ZrO_2, respectively. It is therefore confirmed that Cr_2O_3 is within the mild wear (ploughing) regime, Cr_2O_3-25%TiO_2 is in the crack and powder formation regime, whilst the other samples are approaching or slightly exceeding the threshold between the two.

According to the literature, both the ploughing regime and the crack and powder formation regime are characterized by the release of micrometric or sub-micrometric debris [55,56], which is also consistent with the debris observed in all the present tests (Figure 11B shows the debris released by the Cr_2O_3-25%TiO_2 coating, but identical considerations hold in all cases). Detailed observations of these particles by high-resolution TEM imaging (Figure 11C) show that they usually consist of very fine-grained polycrystals. Selected area diffraction patterns (such as the one shown in Figure 11D) can usually be indexed to an eskolaite-type hexagonal structure. Digital magnification of some of the crystalline areas in Figure 11C also show atomic layers with a spacing of ≈2.5 Å and ≈3.6 Å, matching with the interplanar spacing of the (110) and (012) lattice planes of eskolaite, respectively. It means these are fragments of the coatings, which did not undergo any tribochemical interaction during the sliding contact, as their phase composition is essentially the same as the original coatings. The fine crystallite size is also probably the same as it originally existed in the coatings, and it is a consequence of impact-quenching during spraying.

Debris particles trapped in the contact zone can be compacted back onto the worn surface. Discontinuous surface layers can indeed be identified on all samples, as exemplified by Figure 10B,D, and the detailed view of Figure 11A confirms that they consist of compacted debris particles.

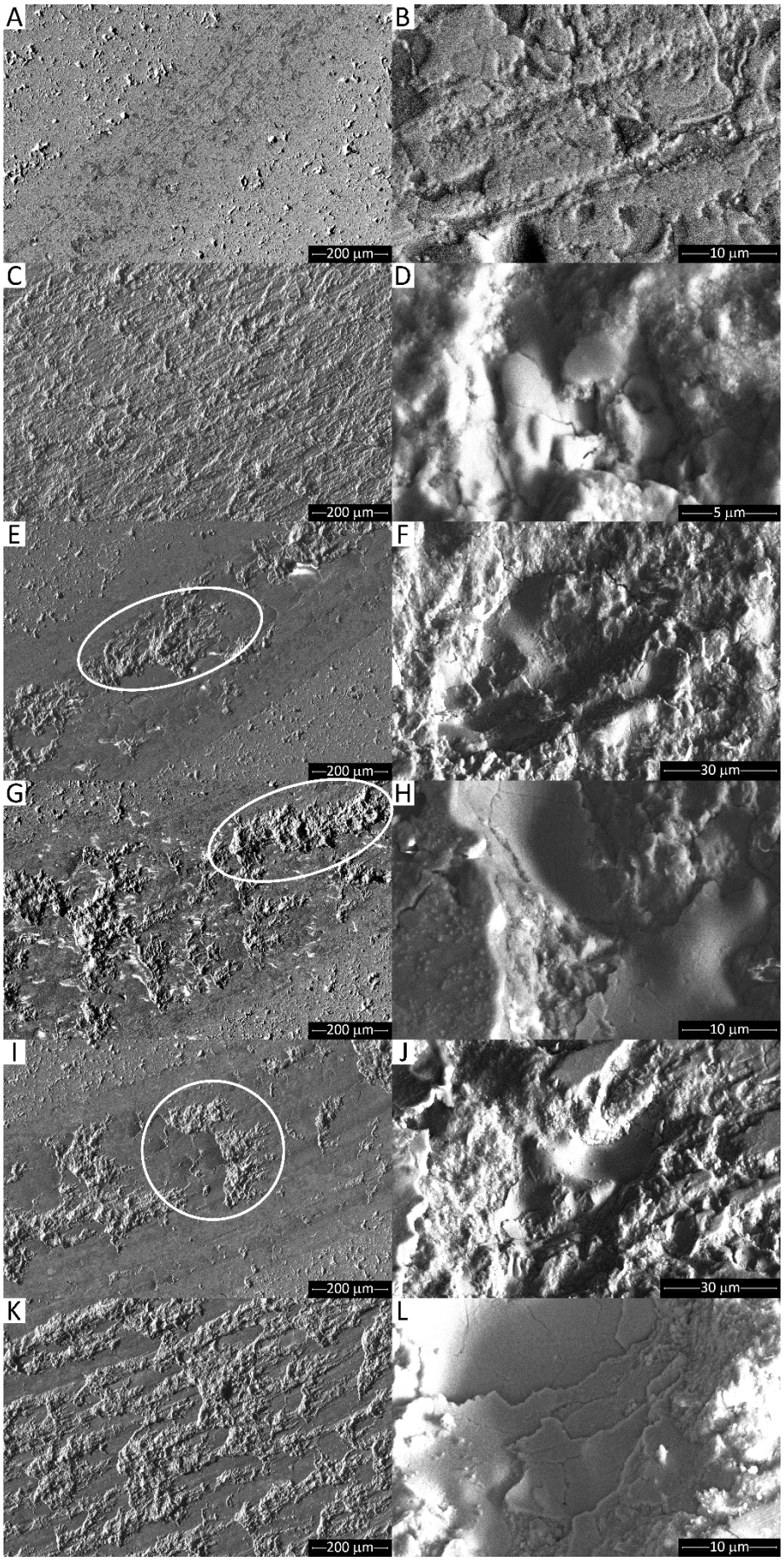
A
200 µm
B
10 µm
C
200 µm
D
5 µm
E
200 µm
F
30 µm
G
200 µm
H
10 µm
I
200 µm
J
30 µm
K
200 µm
L
10 µm

Figure 9: SEM micrographs of worn surfaces after ball-on-disc testing against Al_2O_3 ball: Cr_2O_3 (A,B), Cr_2O_3-25%TiO_2 (C,D), Ruby-L (E,F), Ruby-S (G,H), Cr_2O_3-10%ZrO_2 (I,J), Cr_2O_3-20%ZrO_2 (K,L). Overviews (A,C,E,G,I,K) and details (B,D,F,H,J,L). Circled areas are local spallation events.

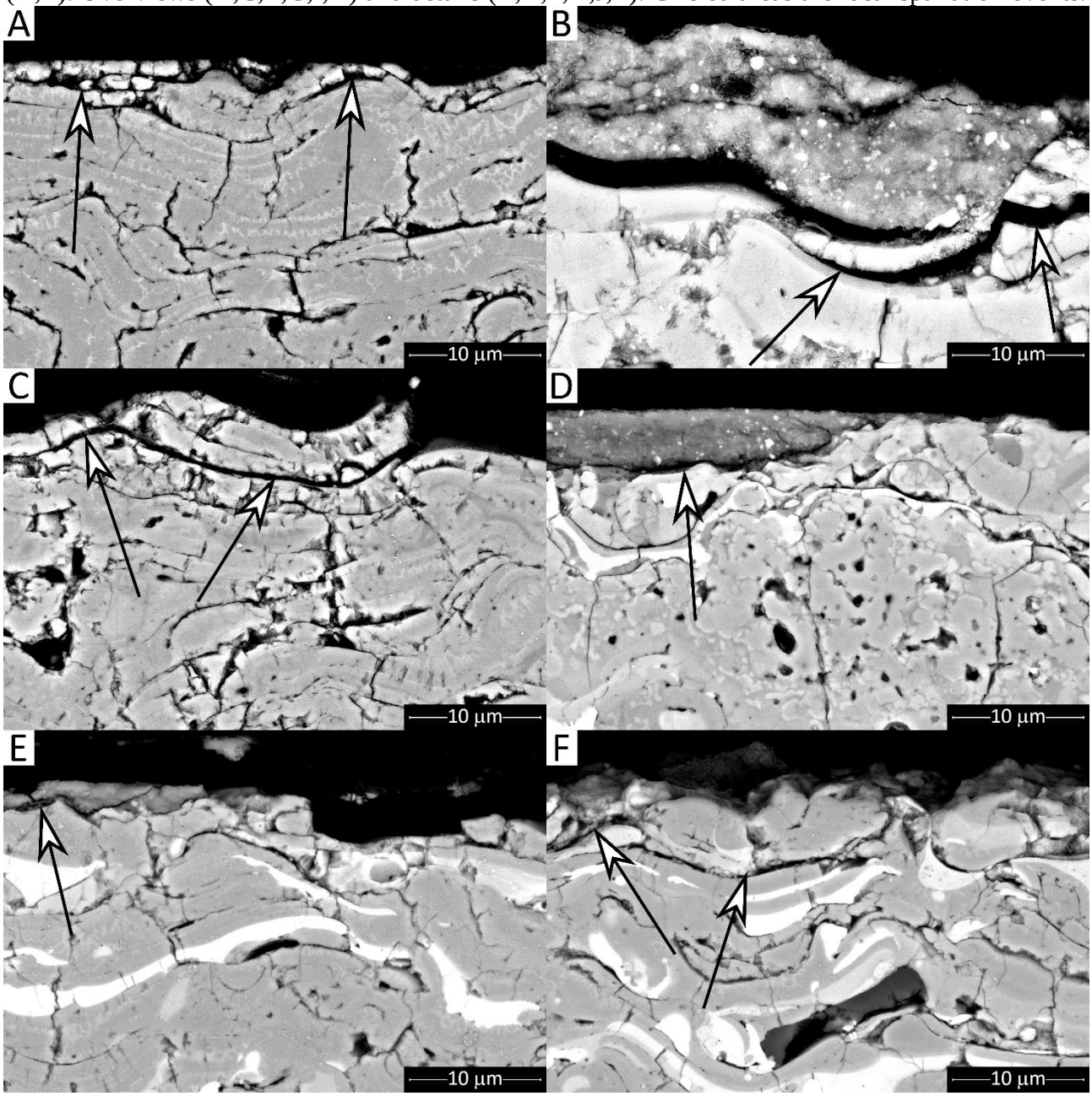

Figure 10: SEM micrographs (backscattered electrons) showing the cross-sections of worn coatings after ball-on-disc testing against Al_2O_3 ball: Cr_2O_3 (A), Cr_2O_3-25%TiO_2 (B), Ruby-L (C), Ruby-S (D), Cr_2O_3-10%ZrO_2 (E), Cr_2O_3-20%ZrO_2 (F). Arrows indicate interlamellar failure.

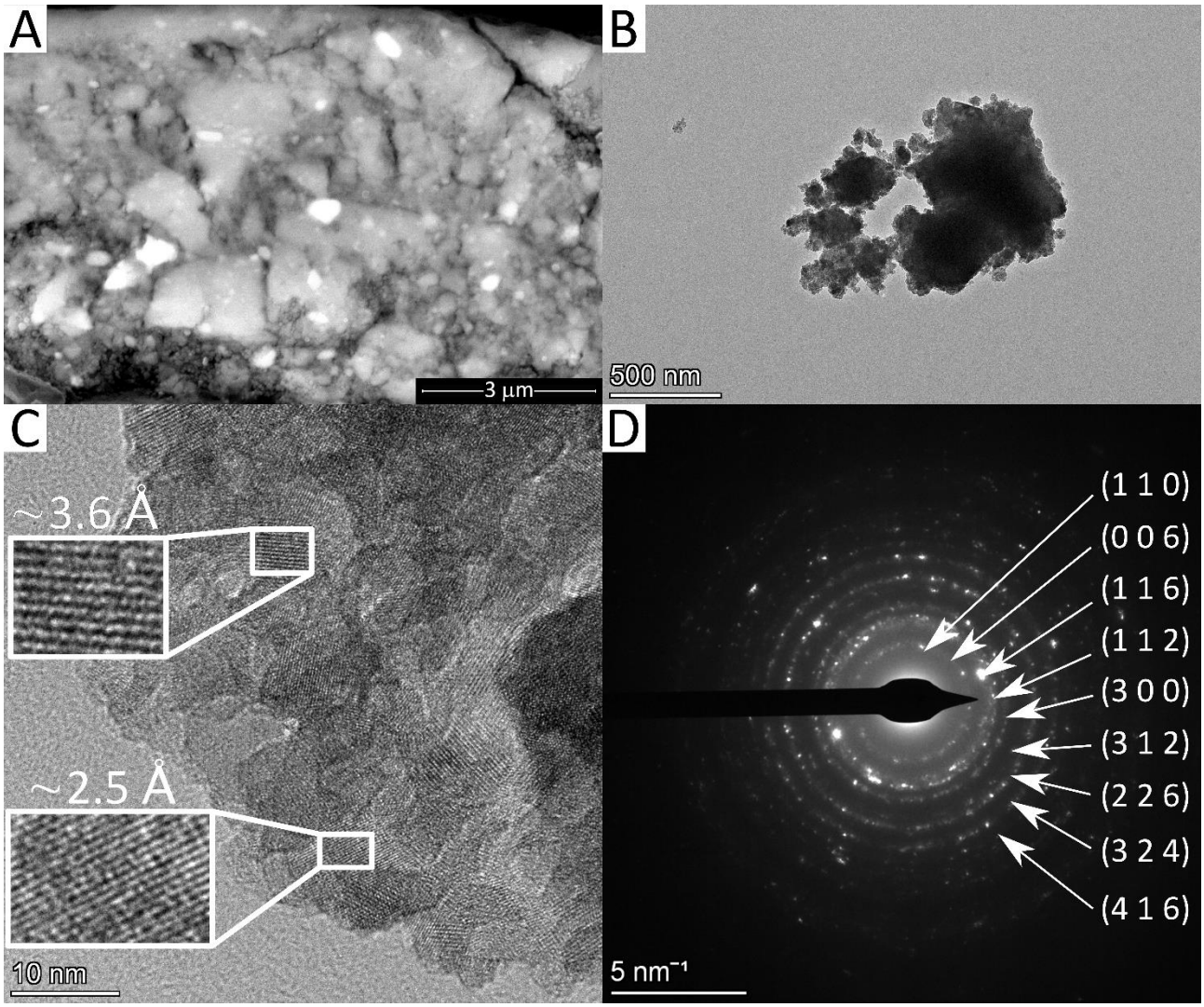

Figure 11: SEM micrograph (backscattered electrons) showing compacted wear debris on the cross-section of the worn Cr_2O_3-20%ZrO_2 coating (A) after ball-on-disc testing against Al_2O_3 ball, TEM micrographs of loose debris particles collected after the same test type onto the Cr_2O_3-25%TiO_2 coating (B: overview, C: high-resolution detail with digitally enlarged insets and indications of the corresponding spacings between atomic layers), and corresponding SAED pattern indexed to the eskolaite structure (JCPDF 38-1479).

3.4.3. Identification of wear mechanisms: sliding wear tests against ZrO_2 ball

SEM observations of worn surfaces (Figure 12A,C,E,G) show that spallation becomes more extensive in tests against ZrO_2 counterparts than it was against Al_2O_3. Cross-sections accordingly show that lamellar spallation is widespread across the entire width of the wear track (Figure 13A,B), even in the case of pure Cr_2O_3 (Figure 13A), which explains why its wear rate increased by almost two orders of magnitude, compared to the tests against Al_2O_3 (Section 3.4.1).

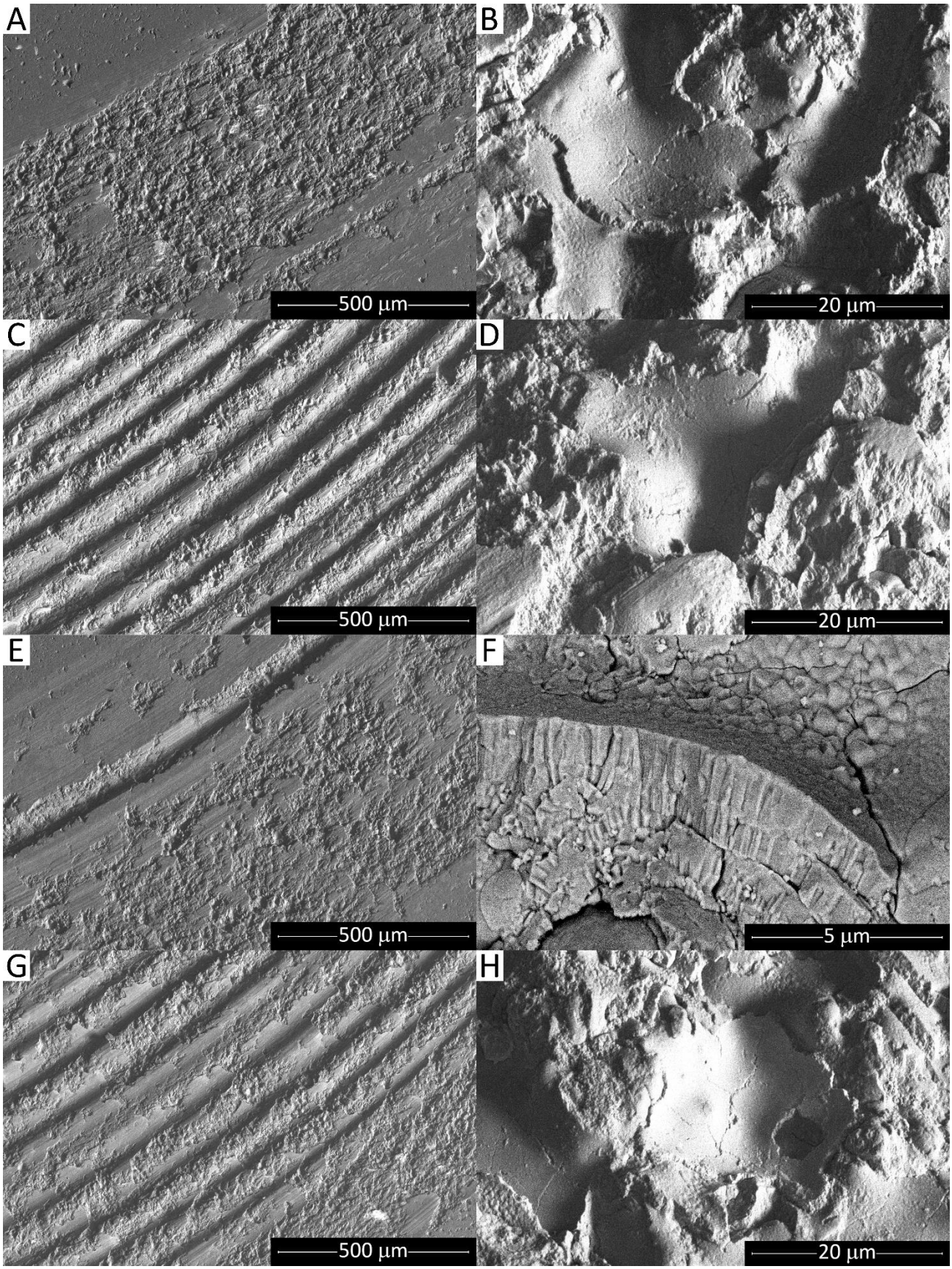

Figure 12: SEM micrographs of worn surfaces after ball-on-disc testing against ZrO_2 ball: Cr_2O_3 (A,B), Cr_2O_3-25%TiO_2 (C,D), Ruby-S (E,F), Cr_2O_3-10%ZrO_2 (G,H). Overviews (A,C,E,G) and details (B,D,F,H).

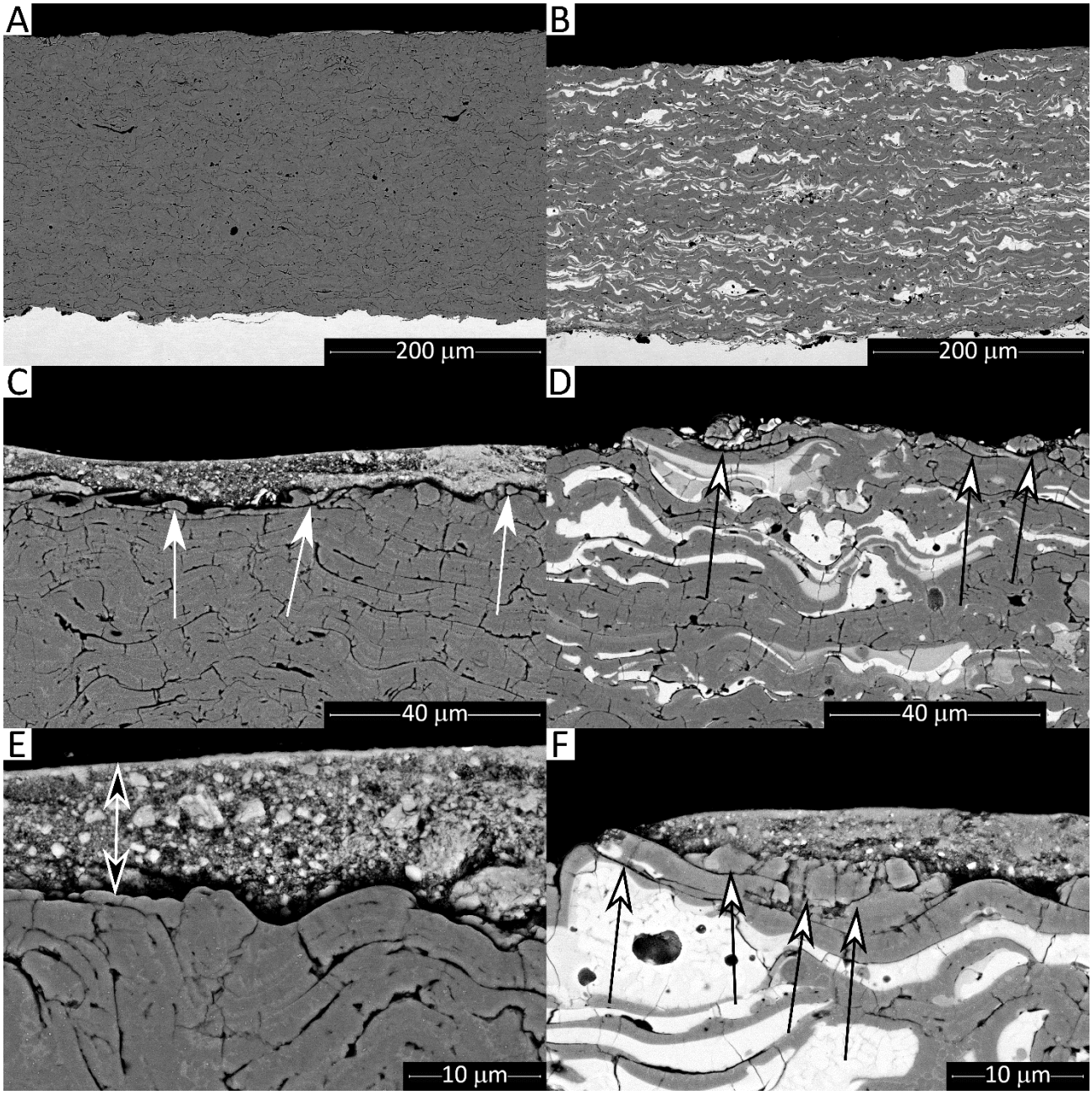

Figure 13: Cross-sectional SEM micrographs (backscattered electrons) of worn coatings after ball-on-disc testing against ZrO_2 ball: Cr_2O_3 (A,C,E), and Cr_2O_3-20%ZrO_2 (B,D,F). Overviews (A,B) and details at intermediate (C,D) and high (E,F) magnifications. Arrows in panels C, D, F show fragmented splats on the worn surface and interlamellar cracks just below them. The arrow in panel E marks a debris layer onto the worn surface.

The dimensionless wear coefficients of the Cr_2O_3, Cr_2O_3-25%TiO_2, Ruby-L, Ruby-S, Cr_2O_3-10%ZrO_2 and Cr_2O_3-20%ZrO_2 samples are 8.5×10^{-5}, 1.7×10^{-3}, 1.5×10^{-4}, 3.4×10^{-4}, 4.5×10^{-4}, 6.0×10^{-4}, respectively. It is therefore confirmed that all samples approach the conditions for the crack and

powder formation regime according to the classification by Kitsunai et al. [55]. However, no long-range crack propagation, i.e. no flake formation, occurs.

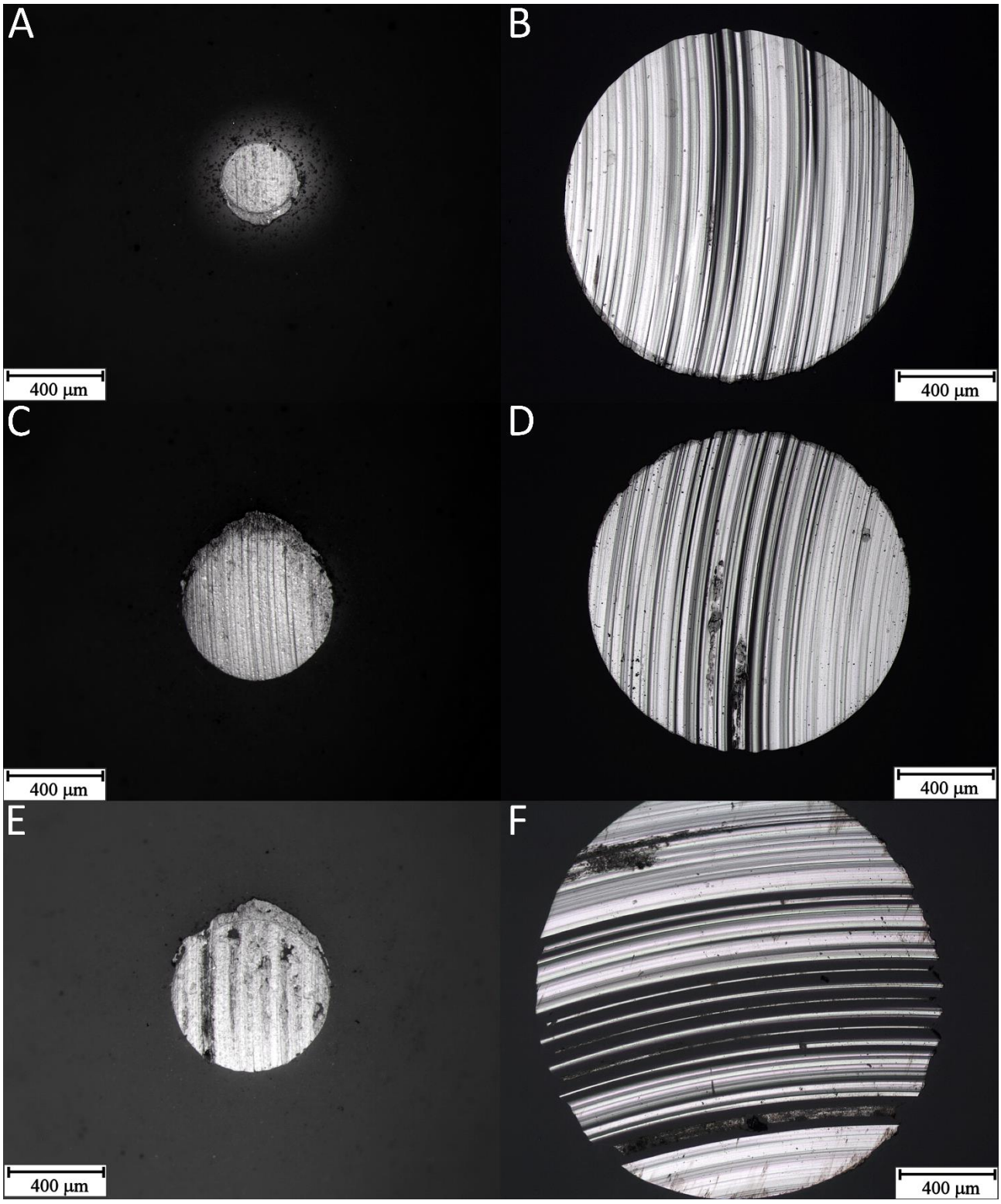

Figure 14: optical micrographs of worn ball surfaces: Al_2O_3 (A,C,E) and ZrO_2 (B,D,F) balls after testing against Cr_2O_3 (A,B), Ruby-S (C,D), Cr_2O_3-10%ZrO_2 (E,F).

In the most severely worn samples, such widespread spallation process degenerated into the formation of large and deep grooves (Figure 12C and G in case of Cr_2O_3-25%TiO_2 and Cr_2O_3-20%ZrO_2, respectively). Spallation is still clearly due to interlamellar failure. Individual lamellae or their fragments are identifiable on worn surfaces (Figure 12B,D,F,H). Splats next to the surface are accordingly seen to have been broken up into fragments, part of which have been removed by the extension of interlamellar cracks. As highlighted by cross-sectional observations (Figure 13C,D,F: fragmented splats and related interlamellar failures are marked by arrows).

Irregular debris layers are also found across the worn surface (Figure 13C,E,F), once again built up by the compaction of particles of micrometre or (mostly) sub-micrometre size, characteristic of the powder formation regime. Figure 13E especially highlights a portion of a debris layer (marked by arrows) that has been compacted on its very surface by the normal and tangential stresses exerted by the pin as well as the local flash heating, whilst the underlying part still consists of individual, non-compacted particles. Figure 13F, on the other hand, shows a more uniformly densified portion of a debris layer.

Observation of worn counterparts explains why lamellar spallation has become much more frequent and widespread in tests against the ZrO_2 ball (Figure 14). Al_2O_3 balls, indeed, wear less, and they develop a smoother surface (Figure 14A,C,E). ZrO_2 balls wear down comparatively more, because of their lower hardness, and they develop deep abrasive grooves (Figure 14B,D,F). Although a worn trace with larger diameter means the average contact pressure between the ball and the coating is lower than it happens with the Al_2O_3 counterbody, this has little practical significance. More important is the fact that the sharp ridges on the grooved surface cause localized spikes of contact pressure and contact stress. Indeed, matching grooves can be produced onto the coating surface through frequent spallation of lamellae, as observed previously. The conditions, therefore, become more severe than they are against Al_2O_3, whose smoother surface does not cause analogous stress concentrations.

3.4.4. Identification of wear mechanisms: rubber wheel abrasion samples

In rubber-wheel abrasion by quartz sand, worn surfaces again exhibit the shape of individual lamellae and fragments thereof (Figure 15A-D), implying brittle interlamellar failure; however, the situation is different from the ball-on-disc tests. Indeed, cross-sectional observations clarify that, especially in the most severely worn samples (Figure 16A,B show the example of pure Cr_2O_3), interlamellar cracks (arrows) extend much longer than it was reported after sliding wear (compare to Figure 10 and Figure 13). They propagate over long distances, affecting multiple lamellar boundaries, and they can be located deep below the surface (especially see the crack marked in Figure 16A). Tong et al. indeed observed similar, long-range crack propagation in plasma sprayed Cr_2O_3 subjected to comparable, high-load abrasion conditions [57]. In addition to those larger cracks, the detail of Figure 16B shows generalized decohesion of the lamellar boundaries for at least half of the residual thickness of the coating.

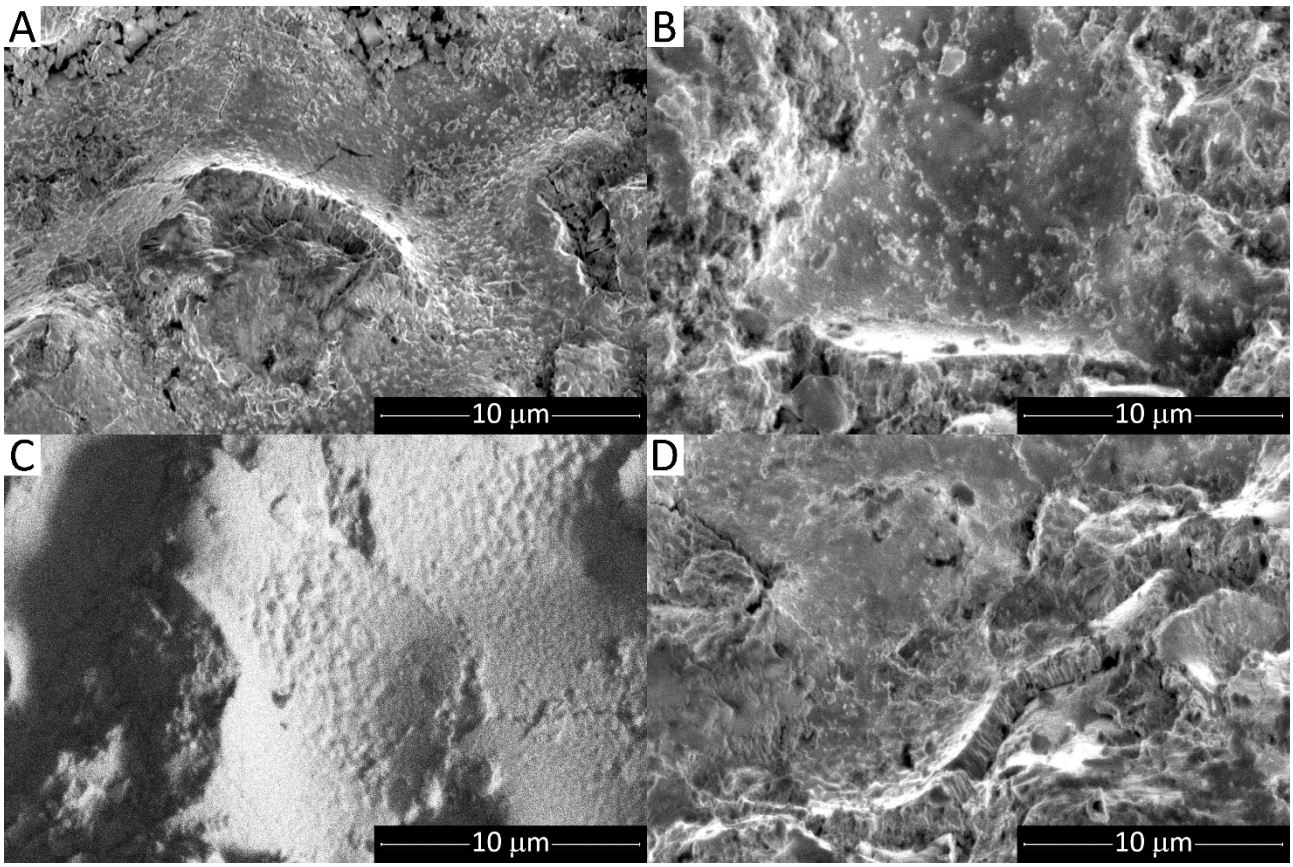

Figure 15: SEM micrographs of worn surfaces after dry sand-rubber wheel abrasion testing: Cr_2O_3 (A), Cr_2O_3-25%TiO_2 (B), Ruby-S (C), Cr_2O_3-10%ZrO_2 (D).

Samples with lower abrasive wear rates, such as the Cr_2O_3-ZrO_2 ones, do not exhibit those large cracks (Figure 16C in case of Cr_2O_3-10%ZrO_2). Lamellar decohesion is also confined to a region closer to the worn surface (Figure 16D). Obviously, these samples also exhibit a greater residual thickness, consistent with the smaller wear rate (compare Figure 16C for Cr_2O_3-10%ZrO_2 and Figure 16A for pure Cr_2O_3).

Rubber-wheel abrasion therefore occurs well within the severe wear regime [53,54], approaching a fully developed flake formation regime according to Kitsunai et al. [55]. Dimensionless wear coefficients are indeed comprised between 3.6×10^{-3} (Cr_2O_3-10%ZrO_2, Cr_2O_3-20%ZrO_2) and 6.7×10^{-3}, thus coming increasingly close to the flake formation range proper (10^{-2} – 10^{-1}).

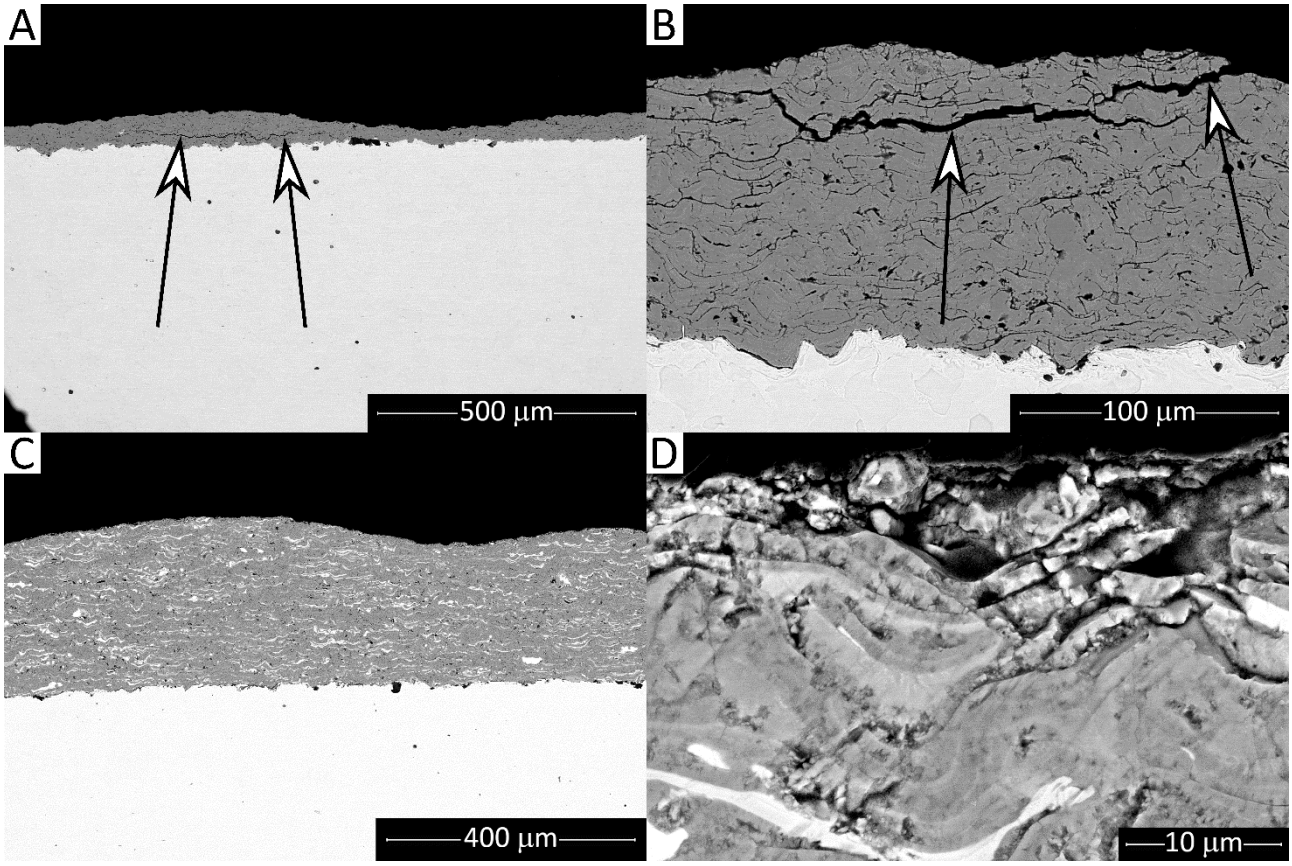

Figure 16: SEM micrographs (backscattered electron images) of the cross-sections of worn samples after dry sand-rubber wheel abrasion testing: Cr_2O_3 (A,B) and Cr_2O_3-10%ZrO_2 (C,D). Arrows indicate extensive sub-surface cracks.

4. Discussion

As stated in the Introduction and in Sections 2.1 and 2.2, the whole samples' manufacturing process, from feedstock selection to spraying, aimed to achieve truly alloyed coatings, as chemically homogeneous as possible, and minimize the influence of factors other than composition on their mechanical properties and tribological behaviour.

The chosen feedstock powders can be regarded as being truly pre-alloyed, based on the results presented in Section 3.1 as well as the additional information provided in Section S1 of the Supplementary Material. Their diverse morphologies might have entailed a risk of introducing differences among the resulting coatings, though that risk was unavoidable, because the agglomerated "Ruby" powders are the only pre-allowed Cr_2O_3-Al_2O_3 feedstock available commercially. However, the coatings (Figure 1B,E,H,K,N,Q) do exhibit very similar microstructures. The stated goal of minimizing any influence from the manufacturing conditions can therefore be regarded as having been mostly achieved.

Considering, more specifically, the tribological results, it must preliminarily be remarked that the findings are strictly valid only for the chosen experimental conditions. However, sliding tests against two distinct counterparts (Al_2O_3 and ZrO_2) returned analogous rankings in terms of wear resistance, despite the differences in the properties and wear behaviour of these counterbodies. This lends some more generality to the discussion.

The tribological results presented in Section 3.4, including data, statistical elaborations (Section 3.4.1), and microstructural analyses (Sections 3.4.2, 3.4.3, 3.4.4), indicate that the coatings' response to sliding or abrasive contacts are controlled by distinct mechanical properties.

Sliding wear tests against the Al_2O_3 counterbody entail a condition where contact is concentrated on very fine asperities: either the asperities on the ball, which, after an initial run-in, develops a smooth worn surface (Figure 14A,C,E), or the equally fine debris (Figure 11B). Their penetration depth into the coating surface is probably not greater than the size of the asperity and/or debris particle itself,

i.e. ≈1 μm. Ashby et al. indeed argued that the contact between hard materials involves asperity of ≈1 μm radius [58]. This penetration depth is comparable to the thickness of a lamella. Therefore, the asperities bend the material before them as they plough through the coating, and "sap" and dislodge lamellae from the surface. With harder coatings, asperities penetrate even less. Indeed, Figure 9B shows that a couple of grooves on the Cr_2O_3 coating after sliding against the Al_2O_3 ball are extremely shallow. The penetration depth and bending strain associated with these shallow grooves is extremely limited and becomes insufficient to dislodge a lamella. The advancing asperities rather induce compression below and before them, which helps keeping the lamellae together, so that the negative influence of the more frequent interlamellar defects in the Cr_2O_3 coating (Section 3.1) is compensated and minimized. As a result, coatings move increasingly towards a mild (ploughing) wear regime as detailed in Section 3.4.2.

This explains why sliding wear resistance primarily correlates with hardness (Section 3.4.1 and Figure 8). Secondarily, it also correlates with the H_{IT}/E^* and H_{IT}^3/E^{*2} ratios. The latter parameters are often employed to interpret the tribological behaviour of coatings and materials [59]. The former is related [60] to the plasticity index (ψ) in the contact between rough surfaces, defined as $\psi = (E^*/H)\sqrt{\sigma/\beta}$ [61], where σ is the standard deviation of the composite roughness profile and β is its average curvature radius. The H_{IT}^3/E^{*2} parameter is related to the normal load at the onset of plasticity in a sphere-on-flat contact, $W \propto R^2 H^3/E^{*2}$ (with R = radius of the sphere), calculated using Hertz's relations and assuming $H \approx 3\sigma_y$ [62]. Therefore, both parameters are related, in different ways, to the ability of the material to sustain contact without plasticization or failure. With the mechanism described above, based on the detachment of individual lamellae (or fragments thereof) by advancing asperities of micrometric size, improved elastic compliance can be an additional benefit, provided that the material is hard enough to limit the overall penetration depth below the size of a splat. More in general, the results of ball-on-disc tests correlate well with indentation testing because the latter probes the same short-range interlamellar cohesion involved in

sliding wear. Beneath a micro-indentation mark in a plasma sprayed ceramic, cracks are formed or opened [63] that are not too different from those leading to the detachment of an individual lamella in Figure 9 and Figure 10.

Irregular layers of compacted debris also form on worn surfaces. These layers do not look much protective against sliding wear: indeed, they were more abundant on the Cr_2O_3-25%TiO_2 coating, which suffers the most severe wear. Pure Cr_2O_3 does not develop a visible tribo-layer, also because it releases very little debris, but a favourable tribological interaction might have occurred. Although TEM analysis only showed eskolaite-based wear debris from this coating, a nanometre-thin surface layer based on higher oxidation states of chromium (e.g. CrO_2, CrO_3) might have been formed, as suggested in [24] based on XPS analysis. This layer might contribute to enhance the wear resistance of the sample. It would explain why pure Cr_2O_3 has much lower wear rate than Ruby-L in dry sliding against Al_2O_3 (Figure 7A) despite their similarity in hardness and H_{IT}/E^*, H_{IT}^3/E^{*2} ratios (Figure 2).

Another possible reason why the sliding wear performances of the pure Cr_2O_3 and Ruby-L coatings differ more than their hardness and hardness/modulus ratios would have suggested might reside in their residual stress state. Whilst it is not the purpose of the present work to provide a detailed stress analysis of all samples, X-ray residual stress measurements were performed on pure Cr_2O_3 and Ruby-L. Experimental methods and results are provided in the Supplementary Material, section S4. Residual stresses on polished Cr_2O_3 and Ruby-L were below the detection limit of the technique, i.e. not more than a few tens of MPa at the most. The extant stress state is, therefore, not a factor behind the observed sliding wear performances. However, it is possible that the Cr_2O_3 coating could develop a thin, compressively-stressed layer during sliding, as previously observed by the authors [64]. A surface layer under compressive stress would also contribute to the especially good sliding wear resistance against Al_2O_3.

Dry particles' abrasion entails completely different contact conditions. In this case, indeed, the coating is indented not by micrometric asperities, but by angular, hard particles of some hundreds of micrometres in size. Resisting this kind of wear is not a matter of preventing micrometric incursions of fine asperities, as it was under sliding wear conditions against Al_2O_3. Abrasion by dry particles causes a long-range brittle failure process that involves the removal of rather large portions of material (Section 3.4.4, Figure 15, Figure 16), i.e. flake formation [55,56].

For this reason, it does not depend much on hardness or any other quantitative parameter obtained by depth-sensing indentation testing, which reflects mostly short-range cohesion.

The abrasive wear mechanism is somewhat similar to what was observed in multipass scratch tracks, where large coatings flakes were also detached by long-range brittle failure (Section 3.3, Figure 3 - Figure 5). Scratch testing indeed simulates an abrasive contact with a hard asperity of size comparable to the silica particles (diamond tip with 200 μm radius). Accordingly, coatings which exhibited fewer spalled areas in the multipass scratch tracks, such as the Cr_2O_3-ZrO_2 ones, do not exhibit the large cracks (Figure 16C,D in case of Cr_2O_3-10%ZrO_2) which were seen after abrasion testing of samples with poorer scratch response, such as pure Cr_2O_3 (Figure 16A,B).

It is especially interesting to note that the resistance to long-range fracture in scratch testing and abrasion testing stands in stark contrast not only with their ranking in hardness, but also with the H_{IT}/E^* and H_{IT}^3/E^{*2} values (Figure 2). Pure Cr_2O_3 and Ruby-L, which possess by far the highest H_{IT}/E^* and H_{IT}^3/E^{*2} ratios, are among the coatings with the most severe damage in both scratch and abrasion tests. It is therefore inferred that scratch tests provide a qualitative ranking of the fracture toughness of the coatings under conditions relevant to tribological (mainly, abrasive) contacts, whilst the H_{IT}/E^* and H_{IT}^3/E^{*2} ratios do not. Chen et al. [60] have also recently argued that H_{IT}/E^* and H_{IT}^3/E^{*2} ratios are no substitutes for fracture toughness of a material, and provided examples of literature data showing no relation, or even an inverse relation, between those parameters and K_{IC}. The examples notably included a thermal spray coating.

An attempt was made to measure indentation fracture toughness quantitatively on the present coatings, to verify the above assumption that scratch testing is closely correlated to this property. However, due to the pre-existing defects in the samples, high-load Vickers indentations produced unusable cracking patterns, a problem which was accordingly reported by Xie and Hawthorne [18] on other plasma sprayed ceramics. The present coatings showed multiple cracks ranging from both the corners and the sides of the indentations, as well as uplifting of material. Such behaviour is incompatible with the fundamental assumption of Palmqvist or half-penny cracking patterns behind all extant indentation fracture toughness models [65–67].

Sliding against the ZrO_2 counterpart seems to effect an intermediate condition between sliding against Al_2O_3 and dry particles' abrasion. The ZrO_2 counterparts wear more severely than do Al_2O_3 ones, and they develop a rougher surface (Section 3.4.3). The ridges on the worn ZrO_2 surface exert a more severe abrasive action than does the smooth Al_2O_3 surface discussed previously, though it is not as severe as that by the coarse quartz particles in the rubber-wheel test. Therefore, lamellar spallation becomes more frequent on the coatings' surface. The wear regime thus shifts more markedly towards crack and powder formation [55] in all cases, though cross-sectional views (Figure 13A,B) do not show the long-range macro-cracks that were found in rubber wheel-tested samples (Figure 16A,B), i.e. no flake formation. Interlamellar cracks do not affect more than one splat at a time (Figure 13C,D,F: arrows) and the material further below the surface is unaffected, i.e. pre-existing defects were not opened up (Figure 13C-F), thus being still somewhat similar to the mechanisms encountered against Al_2O_3 (Figure 16). Therefore, the coatings still rank the same against both counterparts, but toughness starts playing some role. Harder but more brittle coatings like pure Cr_2O_3 and Ruby-L still perform better than do the others, but their performance is proportionally more impaired. It has accordingly been reported that the linear wear rate of Cr_2O_3 coatings increases by two orders of magnitude when the actual contact pressure increases [15]. Moreover, any functional tribofilm or compressively loaded layer that might tend to form on the

surface of the Cr_2O_3 coating (as discussed previously) would be readily removed by the abrasive action of the rough ZrO_2 ball. This would contribute to the comparatively greater impairment of the performance of pure Cr_2O_3, although it is still the most sliding wear resistant of all samples.

5. Conclusions

Coatings based on binary alloys with Cr_2O_3 with either TiO_2, Al_2O_3 or ZrO_2 were obtained by plasma spraying to characterize how alloying additions affect the resistance to sliding and abrasive wear, in comparison to pure Cr_2O_3.

Specifically, pure Cr_2O_3, Cr_2O_3-25%TiO_2, Cr_2O_3-16%Al_2O_3 (Ruby-L), Cr_2O_3-35%Al_2O_3 (Ruby-S), Cr_2O_3-10%ZrO_2 and Cr_2O_3-20%ZrO_2 were considered. All binary feedstock powders did not consist of mechanical blends of pure oxides, but of pre-alloyed materials. Therefore, "truly" alloyed coatings were obtained. Their porosity and microstructure were similar enough, that their mechanical properties and tribological behaviour can reasonably be expected to depend primarily on their composition.

The following conclusions could be drawn:

- Compared with pure Cr_2O_3, the Cr_2O_3-25%TiO_2 and Cr_2O_3-ZrO_2 coatings are less hard (as measured by indentation testing) but tougher (as qualitatively assessed by multipass scratch testing). The Cr_2O_3-16%Al_2O_3 coating has similar hardness and toughness as pure Cr_2O_3; Cr_2O_3-35%Al_2O_3 is softer, though not tougher. The latter effect, however, might also be a consequence of the greater chemical inhomogeneity (particle-to-particle variability in Al_2O_3/Cr_2O_3 ratio) and broad particle size distribution of this feedstock, rather than of its higher average Al_2O_3 content.

  Pure Cr_2O_3 and Cr_2O_3-16%Al_2O_3 coatings also have lower elastic modulus than all other samples and, therefore, much higher H/E and H^3/E^2 ratios.

- Under the present test conditions, sliding wear resistance against ceramic counterparts (Al_2O_3 or Y_2O_3-stabilized ZrO_2 balls) seems to be primarily controlled by hardness. This parameter seems

to be more relevant than the H/E and H^3/E^2 ratios. Hence, pure Cr_2O_3 is the most sliding wear resistant, whilst Cr_2O_3-25%TiO_2 suffers very severe wear rates of $\approx 1.5\times10^{-4}$ $mm^3/(N\cdot m)$ in both cases.

- Sliding wear under the present test conditions occurs in either mild (ploughing) or severe (crack and powder formation) regimes according to the frequency with which individual lamellae are spalled off the surface. This correlates well with the results of micro-indentation testing because the indentation response of a ceramic coating is affected by short-range cohesion.
  The counterpart also has a significant effect on sliding wear rates. For example, as the softer ZrO_2 balls wear down by abrasion, they develop sharp ridges, which, in turn, cause contact stress concentrations on the surface of the coatings. This increases the extent of lamellar spallation, especially in harder but less tough coatings, such as Cr_2O_3 and Cr_2O_3-16%Al_2O_3. Though they are still more sliding wear resistant than other coatings, their wear rates against ZrO_2become more severe and closer to those of the other samples than it happened against the Al_2O_3 counterpart.
- Under dry particles' abrasion conditions as they are effected in this work, on the other hand, wear occurs through a flake formation mechanism and it is controlled by long-range propagation of interlamellar cracks. The ranking among the various samples is almost the opposite as it was under sliding wear conditions: Cr_2O_3 and Cr_2O_3-Al_2O_3 coatings wear more severely, whereas Cr_2O_3-25%TiO_2 and (most of all) Cr_2O_3-ZrO_2 coatings have comparatively lower wear loss, though all wear rates are $\geq 3.5\times10^{-4}$ $mm^3/(N\cdot m)$.
- As depth-sensing micro-indentation probes a short-range mechanical response, parameters obtained from this test, including hardness, elastic modulus, and their ratios, are not good predictors for abrasion resistance. Toughness, instead, becomes the controlling property. Abrasive wear mechanisms can be mimicked through scratch testing. By simulating the sliding of a large, hard asperity on the coating surface, this test elicits the same flaking as it happens in

particles' abrasion. Therefore, the qualitative damage extent observed after a multipass scratch test correlates well with the abrasive wear response. The scratch test provides a qualitative evaluation of toughness in a case where quantitative measurements by indentation fracture toughness methods turned out to be inapplicable.

6. Acknowledgements

The authors are grateful to Ing. Maria Francesca Bonilauri, Ing. Stefania Morelli and Ing. Veronica Testa (Department of Engineering “Enzo Ferrari”, Università di Modena e Reggio Emilia) for their help with the experimental activities.

7. References

[1] M.R. Dorfman, A. Sharma, Thermal Spray Applications in the Paper Production Industry, in: R.C.J. Tucker (Ed.), ASM Handb - Vol 5A Therm Spray Technol, ASM International, Materials Park, OH, USA, 2013: pp. 328–331. doi:10.31399/asm.hb.v05a.a0005743.

[2] A. Sharma, Printing Industry Applications, in: R.C.J. Tucker (Ed.), ASM Handb - Vol 5A Therm Spray Technol, ASM International, Materials Park, OH, USA, 2013: pp. 332–333. doi:10.31399/asm.hb.v05a.a0005744.

[3] D. Lee, Wear-Resistant Coatings, in: R.C. Tucker Jr. (Ed.), ASM Handb - Vol 5A Therm Spray Technol, ASM International, Materals Park, OH, USA, 2013: pp. 253–256. doi:10.31399/asm.hb.v05a.a0005734.

[4] R.B. Heimann, Applications of Plasma-Sprayed Ceramic Coatings, Key Eng Mater. 122–124 (1996) 399–442.

[5] R.C.J. Tucker, Coatings For Centrifugal Pump Components, in: Proc Third Int Pump Symp, Texas A&M University, 1986: pp. 107–110. doi:10.21423/R1068C.

[6] Q.-P. Wu, Z.-H. Deng, F.-X. Lu, Materials for Ceramic Coating/dipped-pitch Graphite Tribo-pairs for High Speed Cigarette Quality Checked Equipment, Mocaxue Xuebao/Tribology. 30 (2010) 135–139.

[7] L. Pawłowski, The Science and Engineering of Thermal Spray Coatings, 2nd ed., John Wiley & Sons Ltd., Chichester, UK, 2008. doi:10.1002/9780470754085.

[8] F.W. Bach, T. Duda, M. Berthold, Food compatibility of thermally sprayed coatings, Schweiss Und Schneiden/Welding Cut. 53 (2001) E2–E5.

[9] P.A. Gaydos, K.F. Dufrane, Lubrication of Ceramics in Ring/Cylinder Applications, in: SAE Int Congr Expo, SAE International, 1989: p. 890888. doi:10.4271/890888.

[10] K.F. Dufrane, Wear Perfomance of Ceramics in Ring/Cylinder Applications, J Am Ceram Soc. 72 (1989) 691–695. doi:10.1111/j.1151-2916.1989.tb06199.x.

[11] F. Rastegar, A.E. Craft, Piston ring coatings for high horsepower diesel engines, Surf Coatings Technol. 61 (1993) 36–42. doi:10.1016/0257-8972(93)90199-X.

[12] R. Köse, L. Urtekin, A. Ceylan, S. Salman, F. Findik, Three types of ceramic coating applicability in automotive industry for wear resistance purpose, Ind Lubr Tribol. 57 (2005) 140–144. doi:10.1108/00368790510601680.

[13] E. Evin, B. Antoszewski, M. Tomáš, J. Tkáčová, D. Draganovská, Tribological Properties of Coatings for Sheet Metal Stamping Dies, Mater Sci Forum. 818 (2015) 69–73. doi:10.4028/www.scientific.net/MSF.818.69.

[14] L. Vernhes, C. Bekins, N. Lourdel, D. Poirier, R.S. Lima, D. Li, J.E. Klemberg-Sapieha, Nanostructured and Conventional Cr2O3, TiO2, and TiO2-Cr2O3 Thermal-Sprayed Coatings for Metal-Seated Ball Valve Applications in Hydrometallurgy, J Therm Spray Technol. 25 (2016) 1068–1078. doi:10.1007/s11666-016-0405-9.

[15] Bu-Qian Wang, Zheng Rong Shui, A. V. Levy, Sliding wear of thermal-sprayed chromia coatings, Wear. 138 (1990) 93–110. doi:10.1016/0043-1648(90)90170-F.

[16] G. Bolelli, V. Cannillo, L. Lusvarghi, T. Manfredini, Wear behaviour of thermally sprayed ceramic oxide coatings, Wear. 261 (2006) 1298–1315. doi:10.1016/j.wear.2006.03.023.

[17] H.X. Zhao, H. Goto, M. Matsumura, T. Takahashi, M. Yamamoto, Slurry erosion of plasma-sprayed ceramic coatings, Surf Coatings Technol. 115 (1999) 123–131. doi:10.1016/S0257-

8972(99)00164-4.

[18] Y. Xie, H.. Hawthorne, The damage mechanisms of several plasma-sprayed ceramic coatings in controlled scratching, Wear. 233–235 (1999) 293–305. doi:10.1016/S0043-1648(99)00211-2.

[19] G. Barbezat, A.R. Nicol, A. Sickinger, Abrasion, erosion and scuffing resistance of carbide and oxide ceramic thermal sprayed coatings for different applications, Wear. 162–164 (1993) 529–537. doi:10.1016/0043-1648(93)90538-W.

[20] R. Westergård, N. Axén, U. Wiklund, S. Hogmark, An evaluation of plasma sprayed ceramic coatings by erosion, abrasion and bend testing, Wear. 246 (2000) 12–19. doi:10.1016/S0043-1648(00)00506-8.

[21] D. Toma, W. Brandl, G. Marginean, Wear and corrosion behaviour of thermally sprayed cermet coatings, Surf Coatings Technol. 138 (2001) 149–158.

[22] V.P. Singh, A. Sil, R. Jayaganthan, Evaluation of dry sliding and slurry erosion behaviour of plasma sprayed nanostructured Cr2O3 –3TiO2 coatings, Tribol - Mater Surfaces Interfaces. 8 (2014) 131–138. doi:10.1179/1751584X13Y.0000000054.

[23] P. Komarov, L. Čelko, D. Jech, M. Papula, K. Slámečka, M. Horynová, L. Klakurková, J. Kaiser, Investigations of Wettability of Wear Resistant Coatings Produced by Atmospheric Plasma Spraying, Solid State Phenom. 270 (2017) 230–235. doi:10.4028/www.scientific.net/SSP.270.230.

[24] H.-S. Ahn, O.-K. Kwon, Tribological behaviour of plasma-sprayed chromium oxide coating, Wear. 225–229 (1999) 814–824. doi:10.1016/S0043-1648(98)00390-1.

[25] Oerlikon Metco - Thermal Spray Materials Guide, (2017). doi:https://www.oerlikon.com/ecomaXL/files/oerlikon_BRO-0001.17_TS_MaterialGuide_EN.pdf.

[26] Höganäs Amperit® 716 Data Sheet, (2020). https://www.hoganas.com/globalassets/download-media/stc/PD-5181.pdf (accessed August

27, 2020).

[27] Praxair Surface Technologies Powder Solutions, (2014). https://www.praxairsurfacetechnologies.com/-/media/corporate/praxairsurface/us/documents/brochures/powders-solutions-catalog.pdf?la=en&rev=26523161064a47f3b8763c5ebf0375ce (accessed August 27, 2020).

[28] L.-M. Berger, S. Saaro, C.C. Stahr, S. Thiele, M. Woydt, Development of ceramic coatings in the Cr2O3-TiO2 system, Therm Spray Bull. 61 (2009) 64–77.

[29] L.-M. Berger, F.-L. Toma, S. Scheitz, R. Trache, T. Börner, Thermisch gespritzte Schichten im System Al2O3-Cr2O3-TiO2 - ein Update, Materwiss Werksttech. 45 (2014) 465–475. doi:10.1002/mawe.201400260.

[30] L.-M. Berger, C.C. Stahr, S. Saaro, S. Thiele, M. Woydt, N. Kelling, Dry sliding up to 7.5m/s and 800°C of thermally sprayed coatings of the TiO2–Cr2O3 system and (Ti,Mo)(C,N)–Ni(Co), Wear. 267 (2009) 954–964. doi:10.1016/j.wear.2008.12.105.

[31] F.-L. Toma, A. Potthoff, M. Barbosa, Microstructural Characteristics and Performances of Cr2O3 and Cr2O3-15%TiO2 S-HVOF Coatings Obtained from Water-Based Suspensions, J Therm Spray Technol. 27 (2018) 344–357. doi:10.1007/s11666-018-0687-1.

[32] A. Potthoff, R. Kratzsch, M. Barbosa, N. Kulissa, O. Kunze, F.-L. Toma, Development and Application of Binary Suspensions in the Ternary System Cr2O3-TiO2-Al2O3 for S-HVOF Spraying, J Therm Spray Technol. 27 (2018) 710–717. doi:10.1007/s11666-018-0709-z.

[33] N. Li, G. Li, H. Wang, J. Kang, T. Dong, H. Wang, Influence of TiO2 content on the mechanical and tribological properties of Cr2O3-based coating, Mater Des. 88 (2015) 906–914. doi:10.1016/j.matdes.2015.09.085.

[34] J.H. Ouyang, S. Sasaki, Effects of different additives on microstructure and high-temperature tribological properties of plasma-sprayed Cr2O3 ceramic coatings, Wear. 249 (2001) 56–66. doi:10.1016/S0043-1648(01)00530-0.

[35] J.H. Ouyang, S. Sasaki, K. Umeda, The friction and wear characteristics of plasma-sprayed

ZrO2-Cr2O3-CaF2 from room temperature to 800°C, J Mater Sci. 36 (2001) 547–555. doi:10.1023/A:1004887413927.

[36] J. Dubsky, P. Chraska, B. Kolman, C.C. Stahr, L.M. Berger, Phase formation control in plasma sprayed alumina-chromia coatings, Ceram - Silikaty. 55 (2011) 294–300.

[37] P. Zamani, Z. Valefi, Microstructure, phase composition and mechanical properties of plasma sprayed Al2O3, Cr2O3 and Cr2O3-Al2O3 composite coatings, Surf Coatings Technol. 316 (2017) 138–145. doi:10.1016/j.surfcoat.2017.03.022.

[38] K. Yang, X. Zhou, H. Zhao, S. Tao, Microstructure and mechanical properties of Al2O3–Cr2O3 composite coatings produced by atmospheric plasma spraying, Surf Coatings Technol. 206 (2011) 1362–1371. doi:10.1016/j.surfcoat.2011.08.061.

[39] B. Dhakar, S. Chatterjee, K. Sabiruddin, Influence of process parameters on the formation of phases and mechanical properties of plasma sprayed Al2O3–Cr2O3 coatings, Mater Res Innov. 21 (2017) 367–376. doi:10.1080/14328917.2016.1265246.

[40] M. Grimm, S. Conze, L. Berger, G. Paczkowski, T. Lindner, T. Lampke, Microstructure and Sliding Wear Resistance of Plasma Sprayed Al_2O_3-Cr_2O_3-TiO_2 Ternary Coatings from Blends of Single Oxides, Coatings. 10 (2020) 42. doi:10.3390/coatings10010042.

[41] S.-N. Chou, J.-L. Huang, D.-F. Lii, H.-H. Lu, The mechanical properties and microstructure of Al2O3/aluminum alloy composites fabricated by squeeze casting, J Alloys Compd. 436 (2007) 124–130. doi:10.1016/j.jallcom.2006.07.062.

[42] Titanium Dioxide, Rutile, (n.d.). http://www.matweb.com/search/DataSheet.aspx?MatGUID=5db351c27977411d930c27de7624012b&ckck=1 (accessed March 18, 2018).

[43] Zirconium Oxide, Zirconia, ZrO_2, (n.d.). http://www.matweb.com/search/DataSheet.aspx?MatGUID=0742ddaddf80467fb6532e025c694e89&ckck=1 (accessed July 26, 2020).

[44] G. Bolelli, B. Bonferroni, J. Laurila, L. Lusvarghi, A. Milanti, K. Niemi, P. Vuoristo,

Micromechanical properties and sliding wear behaviour of HVOF-sprayed Fe-based alloy coatings, Wear. 276–277 (2012) 29–47. doi:10.1016/j.wear.2011.12.001.

[45] A. Kulkarni, J. Gutleber, S. Sampath, A. Goland, W.B. Lindquist, H. Herman, A.J. Allen, B. Dowd, Studies of the microstructure and properties of dense ceramic coatings produced by high-velocity oxygen-fuel combustion spraying, Mater Sci Eng A. 369 (2004) 124–137. doi:10.1016/j.msea.2003.10.295.

[46] G. Antou, G. Montavon, F. Hlawka, A. Cornet, C. Coddet, Exploring Thermal Spray Gray Alumina Coating Pore Network Architecture by Combining Stereological Protocols and Impedance Electrochemical Spectroscopy, J Therm Spray Technol. 15 (2006) 765–772. doi:10.1361/105996306X147045.

[47] S. Beauvais, V. Guipont, M. Jeandin, D. Jeulin, A. Robisson, R. Saenger, Study of the Porosity in Plasma-Sprayed Alumina through an Innovative Three-Dimensional Simulation of the Coating Buildup, Metall Mater Trans A. 39 (2008) 2711–2724. doi:10.1007/s11661-008-9612-4.

[48] G. Bolelli, L. Lusvarghi, T. Manfredini, F.P.P. Mantini, R. Polini, E. Turunen, T. Varis, S.-P.P. Hannula, S.-P.P. Hannula, Comparison between plasma- and HVOF-sprayed ceramic coatings. Part I: microstructure and mechanical properties, Int J Surf Sci Eng. 1 (2007) 38–61. doi:10.1504/IJSURFSE.2007.013620.

[49] G.W. Stachowiak, A.W. Batchelor, Engineering Tribology, Fourth Ed., Elsevier Butterworth-Heinemann, Burlington, MA, USA, 2014.

[50] I.T. Jolliffe, Principal Component Analysis, Second Edi, Springer-Verlag, New York, NY, USA, 2002.

[51] G. Bolelli, L.-M. Berger, T. Börner, H. Koivuluoto, L. Lusvarghi, C. Lyphout, N. Markocsan, V. Matikainen, P. Nylén, P. Sassatelli, R. Trache, P. Vuoristo, Tribology of HVOF- and HVAF-sprayed WC–10Co4Cr hardmetal coatings: A comparative assessment, Surf Coatings Technol. 265 (2015) 125–144. doi:10.1016/j.surfcoat.2015.01.048.

[52] G. Bolelli, L.-M. Berger, T. Börner, H. Koivuluoto, V. Matikainen, L. Lusvarghi, C. Lyphout, N. Markocsan, P. Nylén, P. Sassatelli, R. Trache, P. Vuoristo, Sliding and abrasive wear behaviour of HVOF- and HVAF-sprayed Cr3C2–NiCr hardmetal coatings, Wear. 358–359 (2016) 32–50. doi:10.1016/j.wear.2016.03.034.

[53] K. Adachi, K. Kato, N. Chen, Wear map of ceramics, Wear. 203–204 (1997) 291–301. doi:10.1016/S0043-1648(96)07363-2.

[54] K. Kato, K. Adachi, Wear of advanced ceramics, Wear. 253 (2002) 1097–1104. doi:10.1016/S0043-1648(02)00240-5.

[55] H. Kitsunai, K. Hokkirigawa, N. Tsumaki, K. Kato, Transitions of microscopic wear mechanism for Cr2O3 ceramic coatings during repeated sliding observed in a scanning électron microscope tribosystem, Wear. (1991). doi:10.1016/0043-1648(91)90255-S.

[56] K. Hokkirigawa, Wear mode map of ceramics, Wear. (1991). doi:10.1016/0043-1648(91)90250-X.

[57] Z. Tong, C. Ding, D. Yan, A fracture model for wear mechanism in plasma sprayed ceramic coating materials, Wear. 155 (1992) 309–316. doi:10.1016/0043-1648(92)90090-U.

[58] M.F. Ashby, J. Abulawi, H.S. Kong, Temperature Maps for Frictional Heating in Dry Sliding, Tribol Trans. 34 (1991) 577–587. doi:10.1080/10402009108982074.

[59] A. Leyland, A. Matthews, On the significance of the H/E ratio in wear control: a nanocomposite coating approach to optimised tribological behaviour, Wear. 246 (2000) 1–11. doi:10.1016/S0043-1648(00)00488-9.

[60] X. Chen, Y. Du, Y.-W. Chung, Commentary on using H/E and H3/E2 as proxies for fracture toughness of hard coatings, Thin Solid Films. 688 (2019) 137265. doi:10.1016/j.tsf.2019.04.040.

[61] J.A. Greenwood, J.B.P. Williamson, Contact of Nominally Flat Surfaces, Proc R Soc Lond A Math Phys Sci. 295 (1966) 300–319.

[62] T.Y. Tsui, G.M. Pharr, W.C. Oliver, C.S. Bhatia, R.L. White, S. Anders, A. Anders, I.G.

Brown, Nanoindentation and Nanoscratching of Hard Carbon Coatings for Magnetic Disks, MRS Proc. 383 (1995) 447. doi:10.1557/PROC-383-447.

[63] G. Bolelli, V. Cannillo, L. Lusvarghi, F.P. Mantini, E. Gualtieri, C. Menozzi, An FIB study of sharp indentation testing on plasma-sprayed TiO2, Mater Lett. 62 (2008) 1557–1560. doi:10.1016/j.matlet.2007.09.022.

[64] G. Bolelli, L. Lusvarghi, T. Varis, E. Turunen, M. Leoni, P. Scardi, C.L. Azanza-Ricardo, M. Barletta, Residual stresses in HVOF-sprayed ceramic coatings, Surf Coatings Technol. 202 (2008) 4810–4819. doi:10.1016/j.surfcoat.2008.04.066.

[65] K. Niihara, R. Morena, D.P.. Hasselman, Evaluation of Klc of Brittle Solids By the Indentation Method With Low Crack To Indent Ratios, J Mater Sci Lett. 1 (1982) 13–16. doi:10.1007/BF00724706.

[66] C.B. Ponton, R.D. Rawlings, Vickers indentation fracture toughness test Part 1 Review of literature and formulation of standardised indentation toughness equations, Mater Sci Technol. 5 (1989) 865–872. doi:10.1179/mst.1989.5.9.865.

[67] C.B. Ponton, R.D. Rawlings, Vickers indentation fracture toughness test Part 2 Application and critical evaluation of standardised indentation toughness equations, Mater Sci Technol. 5 (1989) 961–976. doi:10.1179/mst.1989.5.10.961.